Open access • Journal Article • DOI:10.1088/0004-637X/767/2/124

Identifying Elusive Electromagnetic Counterparts to Gravitational Wave Mergers: an end-to-end simulation — Source link

Samaya Nissanke, Mansi M. Kasliwal, Alexandra Georgieva

Institutions: California Institute of Technology, Carnegie Institution for Science

Published on: 23 Oct 2012 - arXiv: High Energy Astrophysical Phenomena

The Astrophysical Journal, 767:124 (21pp), 2013 April 20 doi:10.1088/0004-637X/767/2/124

IDENTIFYING ELUSIVE ELECTROMAGNETIC COUNTERPARTS TO GRAVITATIONAL WAVE MERGERS: AN END-TO-END SIMULATION

Samaya Nissanke[1,2], Mansi Kasliwal[3], and Alexandra Georgieva[1]
[1] Theoretical Astrophysics, California Institute of Technology, Pasadena, CA 91125, USA
[2] JPL, California Institute of Technology, 4800 Oak Grove Drive, Pasadena, CA 91109, USA
[3] The Observatories, Carnegie Institution for Science, 813 Santa Barbara Street, Pasadena, CA 91101, USA

Received 2012 September 7; accepted 2012 December 18; published 2013 April 4

ABSTRACT

Combined gravitational wave (GW) and electromagnetic (EM) observations of compact binary mergers should enable detailed studies of astrophysical processes in the strong-field gravity regime. This decade, ground-based GW interferometers promise to routinely detect compact binary mergers. Unfortunately, networks of GW interferometers have poor angular resolution on the sky and their EM signatures are predicted to be faint. Therefore, a challenging goal will be to unambiguously pinpoint the EM counterparts of GW mergers. We perform the first comprehensive end-to-end simulation that focuses on: (1) GW sky localization, distance measures, and volume errors with two compact binary populations and four different GW networks; (2) subsequent EM detectability by a slew of multiwavelength telescopes; and (3) final identification of the merger counterpart amidst a sea of possible astrophysical false positives. First, we find that double neutron star binary mergers can be detected out to a maximum distance of 400 Mpc (or 750 Mpc) by three (or five) detector GW networks, respectively. Neutron-star–black-hole binary mergers can be detected a factor of 1.5 further out; their median to maximum sky localizations are 50–170 deg^2 (or 6–65 deg^2) for a three (or five) detector GW network. Second, by optimizing depth, cadence, and sky area, we quantify relative fractions of optical counterparts that are detectable by a suite of different aperture–size telescopes across the globe. Third, we present five case studies to illustrate the diversity of scenarios in secure identification of the EM counterpart. We discuss the case of a typical binary, neither beamed nor nearby, and the challenges associated with identifying an EM counterpart at both low and high Galactic latitudes. For the first time, we demonstrate how construction of low-latency GW volumes in conjunction with local universe galaxy catalogs can help solve the problem of false positives. We conclude with strategies that would best prepare us for successfully identifying the elusive EM counterpart of a GW merger.

Key words: binaries: close – catalogs – gamma-ray burst: general – gravitational waves – stars: neutron – surveys

Online-only material: color figures

1. INTRODUCTION

Our understanding of astrophysical processes in strong-field gravity regimes is limited by the nature of the electromagnetic (EM) force and current instrument sensitivity. Low rates, short timescales, high energies, and interactions with their environments characterize transient strong-field gravity events in the universe. Such events provide us with a brief window to study the interplay of fundamental physical processes. In this respect, gravitational wave (GW) astronomy should allow for the study of such events in the universe, currently inaccessible through EM observations. With GW observations alone, we may infer the physical and geometric properties of individual sources and determine event rates. Furthermore, the combination of GW and EM measurements will lead to improved understanding of astrophysical processes in the strong-field gravity regime and also to construction of a demographic census of different strong-field gravity events (e.g., Bloom et al. 2009; Kulkarni & Kasliwal 2009; Phinney 2009). A challenging goal in this respect is to localize and identify a strong-field gravity event in the universe jointly by GW and EM measurements.

Within the next decade, a worldwide network of advanced versions of ground-based GW interferometers—LIGO in the US and possibly India (Barish & Weiss 1999; Sigg & the LIGO Scientific Collaboration 2008; Sathyaprakash et al. 2012), Virgo in Italy (Accadia et al. 2011), and KAGRA in Japan (Somiya 2012)—will become operational within the frequency range of 10 Hz to a few kHz. At these frequencies, inspiraling and merging compact-object binaries, composed of neutron stars (NSs) and/or stellar-mass black holes (BHs), are expected to be among the most numerous and strongest GW-emitting sources. Mergers of NS–NS and NS–BH binaries, where at least one object includes initially neutron-rich material and possibly strong magnetic fields, are expected to emit in both GWs and EM waves.

GW detections of compact binary mergers are anticipated to become *routine* by the end of this decade. Based on the observed Galactic binary pulsar distribution and population synthesis results, predicted event rates for NS–NS binary mergers range from 0.4 to 400 yr^{-1} (with 40 being the mean value quoted in Abadie et al. 2010) detectable by an advanced GW three-detector network to distances of several hundred megaparsecs. Based solely on population synthesis results due to an absence of observed NS–BH systems, predicted event rates range from 0.2 to 200 yr^{-1} for NS–10 $M_\odot$ BH binary mergers with detectable distances >1 Gpc.[4]

EM detections of compact binary mergers are still a matter of debate. There is growing evidence that short–hard gamma-ray bursts (SGRBs) represent the small fraction of NS–NS or NS–BH mergers beamed toward us (see, e.g., Nakar 2007; Berger 2011). Joint GW and EM observations can unequivocally test this hypothesis and illuminate the nature of the central

---

[4] The particular value of 10 $M_\odot$ is chosen to be representative of stellar-mass BHs; however, as discussed in Section 2, it is unclear whether a NS–10 $M_\odot$ BH binary merger will produce an EM signature. We use NS–5 $M_\odot$ BH in this paper.

engine and collimated outflows. Additionally, extensive theoretical modeling is underway to predict the EM signature for post-merger ejecta, produced from all mergers, which is gravitationally unbound to the final remnant BH. For instance, a plausible EM counterpart in the optical or near-infrared, referred to as a kilonova, macronova, or mini-supernova, may be powered by weak radioactive decay arising from any neutron-rich ejecta (e.g., Li & Paczyński 1998; Kulkarni 2005; Metzger et al. 2010; Chawla et al. 2010; Roberts et al. 2011; Piran et al. 2013; Wanajo & Janka 2012).

To observe in both GWs and EM waves, two scenarios exist that depend critically on the timescale of the EM emission with respect to the NS binary merger time. They are as follows: (1) a GW event is first detected and is then followed by a slew of multi-wavelength EM telescopes and (2) an EM observation is seen prior to, or coincident with, a GW measurement. Such "GW-triggered" and "EM-triggered" searches were implemented with the enhanced LIGO and Virgo interferometers before they halted for upgrades to their advanced versions (Abadie et al. 2012a, 2012b; LIGO Scientific Collaboration et al. 2012a, 2012b). In this paper, we focus on the first scenario, in which we first observe the inspiral of a NS binary in GWs, and we then detect their EM counterparts using multiwavelength EM observatories. This scenario leverages the instantaneous all-sky visibility of GW detectors in comparison to the narrow field-of-view (FoV) of EM facilities. Due to the improvement in the instrument sensitivity and hence GW-detectable distance by an approximate factor of 10, EM follow-up in the advanced GW interferometric era presents a new set of challenges to that faced by the initial versions.

Here, we view the EM follow-up of a GW event in three steps: (1) localization on the sky with GW measured areas and volumes using a network of GW interferometers, (2) detectability using different multiwavelength EM facilities, particularly the optical, and (3) strategies to reduce the number of false-positive signatures that might mimic an EM counterpart of a NS binary merger within the same GW localization volume.

Several works over the past few years have begun to explore GW sky localization. A single GW interferometer has poor directional sensitivity for transient signals because of its broad antenna function. Localizing any source on the sky depends primarily on triangulating the GW signal's arrival times at detectors using networks of three or more GW interferometers. Studies estimate sky localization errors for unmodeled and modeled GW sources to vary from less than one to a few hundred square degrees using networks of GW interferometers (Fairhurst 2011, 2012; Wen & Chen 2010; Nissanke et al. 2011; Klimenko et al. 2011; Schutz 2011; Veitch et al. 2012). Previous works assume that the GW source is fixed at high signal-to-noise ratio (SNR) or distance, and use analytically derived Fisher matrix estimates (e.g., Fairhurst 2011, 2012; Wen & Chen 2010; Klimenko et al. 2011; Schutz 2011; Veitch et al. 2012). However, a significant fraction of expected signals will be at SNR threshold and degeneracies between parameters in the predicted GW strain become important. In contrast to earlier work, we compute explicit GW errors of volumes, distances, and sky errors using the full predicted GW wavestrain for astrophysically distributed NS binary mergers.

Recent works have also begun to explore EM detectability. Some papers take a statistical approach; for instance, Singer et al. (2012) divide sky localization errors between telescopes and advocate a coordinated response while Nuttall & Sutton (2010) assign a probabilistic ranking statistic for host galaxies out to 100 Mpc. Some focus on a particular wavelength (e.g., X-rays; Kanner et al. 2012). Metzger & Berger (2012) seek to identify the most promising among proposed EM counterparts by defining cardinal virtues and discounting follow-up in optical and radio compared to γ-rays. They assume single numbers for detectable distances[5] and sky localization. Here, we take a different approach. We simulate an astrophysical NS binary population and consider the full range of distances, localizations, and GW networks. We quantitatively divide the pie of binaries by beaming angle, Galactic latitude, and distance. We then consider the challenges and optimal multi-wavelength strategies in each slice.

In this work, we present an end-to-end simulation with the following five steps.[6] First, we construct astrophysically motivated distributions of NS–NS and NS–5-$M_\odot$-BH binary mergers detectable by different GW networks using different triggering criteria (Section 2). Each binary will have specific geometric properties: an orientation, a sky position, and a luminosity distance. Second, by simulating GW data streams using analytically modeled GW strains, we estimate source parameters measured by different GW networks. For parameter estimation, we use MCMC methods developed in Nissanke et al. (2010, 2011; henceforth N10 and N11, respectively). As well as estimating the sources' sky areas, we compute the sky volume errors (Section 3). We summarize the distributions of sky errors, volumes, and distances for NS binary merger populations detected by different networks and different trigger criteria (Section 4). Third, armed with localizations and distances of each binary in the simulation, we assess the feasibility of detecting an EM counterpart with a wide suite of current and planned EM facilities. We pay close attention to the trade-off between depth and area given finite telescope time (Section 5). Fourth, using detailed case studies, we present the challenges and discuss possible strategies to pinpoint the GW event among the anticipated few to many false-positive transients in different wavelengths (Section 6). In conjunction with a galaxy catalog, we discuss how fractional reductions in volume error can reduce the overall number of false-positive transients within a GW-localized event. Finally, we conclude with strategies that maximize the success of identifying EM counterparts of GW events (Section 7).

2. CONSTRUCTION OF TWO NS BINARY MERGER CATALOGS

We construct two distinct catalogs with either 4×10^4 NS–NS or 3×10^4 NS–5-$M_\odot$-BH binary populations.[7] For every binary

---

[5] For clarity, we define here different distance definitions that are used in the literature. By *average detectable* distance, we refer to the *average* distance that a single GW interferometer with idealized Gaussian instrument noise can observe NS binary inspirals averaged over all possible sky positions and binary orientations. On the other hand, the *horizon* distance refers to the maximum detectable distance that a single GW interferometer with idealized Gaussian noise can detect a NS binary event that is located directly above the interferometer and is optimally orientated face-on. The horizon distance improves on the average detectable value by an approximate geometric factor of ∼2.24 (e.g., see Finn & Chernoff 1993).

[6] Discussed in detail throughout the paper, our results are necessarily limited by the assumptions we make; for instance, we assume that joint observable GW–EM events are non-spinning NS–NS and NS–5 $M_\odot$ binary systems, and idealized Gaussian GW interferometric noise and observing conditions at optical telescopes.

[7] We choose a sufficiently large number of binary systems in each catalog such that GW networks will detect a sizable number of systems; the particular values of 4×10^4 NS–NS or 3×10^4 NS–5-$M_\odot$-BH systems are specified somewhat arbitrarily.

in each catalog, we assign physical and geometric source properties as described below. In this study, physical source parameters are the individual compact objects' masses m_1 and m_2 (the spin of the NS and/or BH is assumed to be negligible). The geometric source parameters comprise the luminosity distance D_L, the sky position in spherical polar coordinates (which points from the center of the Earth to the binary) $\mathbf{n} \equiv (\theta, \phi)$, and the binary's inclination angle $\cos\iota = \hat{\mathbf{L}} \cdot \hat{\mathbf{n}}$, where $\hat{\mathbf{L}}$ is the unit vector normal to the binary's orbital plane. The colatitude θ and longitude ϕ describe $\mathbf{n}$, and are related to the declination δ and right ascension α, by $\theta = \pi/2 - \delta$ and $\phi = \alpha - \mathrm{GAST}$, respectively, where GAST is Greenwich Apparent Sidereal Time (see N10 for details on the binary's and Earth's coordinate systems used in this work). Let us consider now how we assign specific source parameters to each binary.

Regarding the physical source parameters, we assume that each NS has a physical mass of 1.4 $M_\odot$, each BH has a physical mass of 5.0 $M_\odot$, and that the objects are non-spinning. In practice, we expect the NS binary population in the universe to have continuous NS and/or BH mass distributions. In the case of NS–BH binaries, instead of the fiducial 10 $M_\odot$ BH used in standard GW literature, we choose BHs with a small enough mass that the NS companion does not plunge directly into the gravitational potential well of the central BH. Therefore, we can expect some tidal disruption of the NS to occur and to observe an accompanying EM counterpart. Tidal disruption occurs if the tidal disruption radius is greater than the BH's innermost circular orbit (ICO); the tidal disruption radius is a function of the BH's spin, the NS's equation of state, and the binary's mass ratio (see discussions in, e.g., Taniguchi et al. 2007; Shibata & Taniguchi 2008; Shibata et al. 2009; Kyutoku et al. 2011; Foucart et al. 2011; Foucart 2012). The ICO describes the last stable circular orbit of the binary system prior to the merger and can be approximated to a test particle's innermost stable circular orbit (ISCO) radius of $6\,GM/c^3$ for a non-spinning BH, where G is the gravitational constant, c is the speed of light, and M is the BH's mass (Shapiro & Teukolsky 1983). In addition, in the actual universe, we expect BHs in NS–BH systems to have considerable spin, and tidal disruption may occur for a NS orbiting prograde around a highly spinning 10 $M_\odot$ BH (Foucart et al. 2011). We choose NS–NS and NS–BH systems with binary separations of $1.0 \times 10^{-3}\ R_\odot$ and $1.4 \times 10^{-3}\ R_\odot$, respectively, to ensure that they will merge within the system's characteristic gravitational radiation timescale (Shapiro & Teukolsky 1983).

Regarding geometric source parameters, for each of our two catalogs, we distribute either 4×10^4 NS–NS binaries or 3×10^4 NS–BH binaries out to $z = 0.5$ ($\sim$2.82 Gpc assuming a ΛCDM universe given in Komatsu et al. 2009). Each binary in a catalog is associated with a random orientation such that $p\,(\cos\iota) \propto$ const with $\cos\iota \in [-1, 1]$, and a random sky position such that $p\,(\cos\theta) \propto$ const with $\cos\theta \in [-1, 1]$ and $p\,(\phi) \propto$ const such that $\phi \in [0, 2\pi]$.

For those NS binary merger events with distances <200 Mpc, we assume that the spatial distribution of NS binaries traces host galaxy light. We use a "Census of the Local Universe" (CLU) with information compiled from different galaxy catalogs that provide B-band luminosities (e.g., HyperLEDA, NED, EDD; see Kasliwal 2011 for details). The probability that a binary is located in a particular galaxy is weighted by the B-band luminosity of that galaxy in CLU. The size of the galaxy is assumed to be three times the size given by the surface brightness contour at apparent magnitude 25 arcsec^{-2} in CLU. B-band luminosity incompleteness is taken into account by dividing the catalog into 10 Mpc bins and choosing random positions for galaxies that represent the missing luminosity.

Finally, for those binaries located with distances >200 Mpc, we assume that the NS binary merger distribution has a constant comoving volume density in a ΛCDM universe (Komatsu et al. 2009).

In summary, we construct two catalogs of 4×10^4 NS–NS and 3×10^4 NS–5-$M_\odot$-BH binary populations, where each binary is described by its set of physical and geometric source parameters: $\{m_1, m_2, D_L, \cos\iota, \cos\theta, \cos\phi\}$.

3. GW DETECTABILITY AND PARAMETER ESTIMATION METHOD

With the geometric and physical source parameters in hand for each binary, we can simulate the predicted GW strain emitted for every inspiraling NS binary in our two catalogs defined above. With knowledge of anticipated GW interferometric noise curves and by assuming idealized Gaussian instrument noise, we can simulate the predicted GW data stream measured at a particular GW interferometer. Therefore, by matched filtering a GW detector output with a theoretically predicted GW waveform, measurements of GWs will allow us to: (1) detect NS–NS and NS–BH binary inspirals and mergers and (2) extract the physical and geometric properties of the source. We first review our understanding of GW waveforms, and then introduce the particular GW waveform that we use. Second, we outline the principles of matched filtering used when detecting and estimating parameters of the GW source. Finally, we describe the different GW networks considered and the three triggering criteria used to construct different GW-detected NS binary merger populations. Further details can be found in N10 and N11.

3.1. GW Waveform

Turning to models of GW emission and dynamics, we view the GW waveform for merging compact binaries in terms of three phases; the inspiral, merger, and ringdown. The inspiral phase, describing the loss of energy and angular momentum of the binary due to GWs, can be modeled accurately using the post-Newtonian (PN) approximation in general relativity. The PN approximation is an expansion in $\sim v^2/c^2$, where v is the characteristic orbital speed for gravitationally bound systems. The state-of-the-art accuracy for non-spinning inspiraling binaries is 3.5PN, corresponding to an order of $\mathcal{O}(1/c^7)$ in a PN expansion (e.g., Blanchet 2006). At 3.5PN, NSs, and/or BHs are modeled using the "point"-particle ("δ"-function) description, with finite-size effects being formally negligible up to 5PN. However, several orbits prior to the merger of the two bodies, the weak-field PN approximation is no longer valid, and we require computationally expensive, numerical simulations that model the merger phase by directly solving Einstein field equations (see, e.g., Pretorius 2005). After the two bodies have merged into a final single BH, perturbation techniques of a Kerr BH describe the ringdown.

We make two important assumptions for the GW waveform used in our work. First, we assume that only the inspiral phase models the GW signal in this work. This is because the inspiral phase contributes to the majority of the signal accumulated in the frequency band of advanced interferometers for NS–NS and several stellar-mass NS–BH systems (see Flanagan & Hughes 1998). Typically, the inspiral phase of NS binaries lasts from a few to tens of minutes in the interferometer's frequency band

(Cutler et al. 1993). Second, we neglect the spin of NSs and BHs in our analysis. We expect NSs to have small spins in NS–NS and NS–BH systems. In contrast, BHs in NS–BH systems should have moderate to large spins. In the case of NS–10-$M_\odot$-BH (with high spin) binaries, we expect spin precessional effects to increase the dimensionality of the parameter space and to modulate the GW waveform significantly, which in some cases can improve GW sky localization (van der Sluys et al. 2008; Raymond et al. 2009). Consequently, neglecting the merger phase and assuming non-spinning binary systems will introduce systematic errors when estimating source parameters. However, as most GW detections will be at threshold, we estimate that statistical errors will dominate over GW waveform systematic errors for the majority of NS binary inspirals.

The GW inspiral encodes a combination of the NS binary's physical and geometric properties such as its redshifted masses, its luminosity distance, its orientation, its source position, as well as the time and phase of coalescence. Specifically, the predicted GW waveform at a particular detector a comprises the linear sum of the two GW polarizations h_+ and $h_\times$ weighted by the two antenna functions F_+ and $F_\times$, and is given by

$$\begin{aligned} h_a &= D_a^{ij} h_{ij} \\ &\equiv e^{-2\pi i (\mathbf{n}\cdot\mathbf{r}_a) f} (F_{a,+} h_+ + F_{a,\times} h_\times)\,, \end{aligned} \tag{1}$$

where D_a^{ij} is the detector's response tensor, and $\mathbf{r}_a$ denotes the detector's position in spherical polar coordinates from Earth's center. The scalar product $\mathbf{n}\cdot\mathbf{r}_a$ denotes the time-of-flight of the signal from the source to the GW interferometer. In our work, we use a GW waveform in the frequency domain, $h_+(f)$ and $h_\times(f)$, where the stationary-phase approximation assumes that $(df/dt)/f \ll f$ (Droz et al. 1999). The GW waveform used is accurate up to 3PN order in its phase (this improves the accuracy of the waveform used in N10 and N11) and Newtonian in its amplitude. The 3.5PN GW phase depends on physical source parameters such as the redshifted chirp mass $\mathcal{M}_z = (1+z)\mathcal{M}_c = (1+z)\, m_1^{3/5}\, m_2^{3/5} / (m_1+m_2)^{1/5}$, z is the binary's redshift (henceforth the notation $\mathcal{M}_c$ refers to the physical non-redshifted chirp mass), and $\mu_z = (1+z)\, m_1 m_2 / (m_1+m_2)$ is the redshifted reduced mass. The 3.5PN phase also includes t_c and Φ_c, which are integration constants and define the time and phase of coalescence, respectively. In contrast, the Newtonian-order GW amplitude is a function of the GW frequency derivative $\dot{f}$ or so-called chirp (itself a function which depends at Newtonian order on the $\mathcal{M}_z$ and at higher 1PN order on the μ_z), and of the geometric parameters such as the binary's $\cos\iota$, D_L and its source position $(\cos\theta, \phi)$. Physical source parameters that appear in the GW phase and $\dot{f}$ can be determined to a high accuracy for NS binaries because from thousands to tens of thousands of inspiral GW cycles could sweep up in the frequency band of the advanced GW detectors. However, only weak constraints on geometric source parameters, such as $(\cos\iota, D_L)$, are possible because of strong degeneracies that exist between parameters appearing in the GW amplitude. This is the case for the majority of threshold-detected GW events (see N10 for further discussion). However, for $(\cos\theta, \phi)$, differences in time-of-flight among detectors in the network dominate over GW amplitude effects when reconstructing the event's sky position. We terminate our inspiral waveform abruptly at the ISCO, $f_{\rm ISCO} = (6\sqrt{6}\pi M_z)^{-1}$, where $M_z = (1+z)(m_1+m_2)$ is the redshifted total mass of the system. Such an abrupt cutoff of the GW waveform should have little impact on matched filtering for NS–NS binaries where $f_{\rm ISCO}$ occurs at high frequencies with poor detector sensitivity (see Figure 1). In contrast, for higher total mass NS–BH binaries, $f_{\rm ISCO}$ lies within the frequency band with high detector sensitivity and such an unphysical cutoff will introduce non-negligible systematic errors. Finally, we assume that calibration measurement errors are negligible (Lindblom 2009; Vitale et al. 2012).

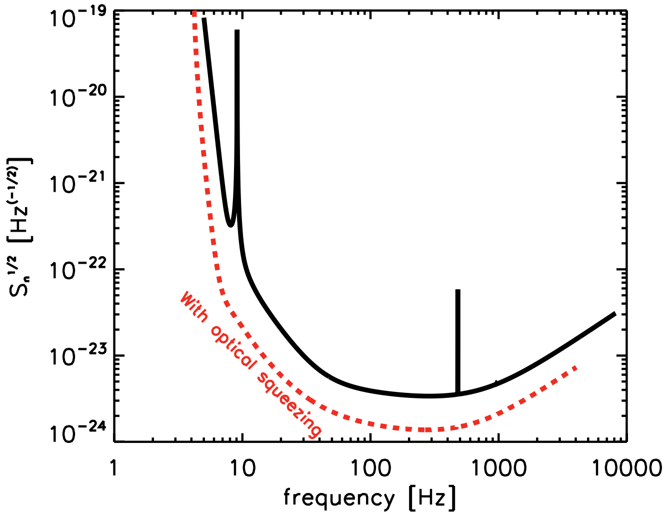

Figure 1. Anticipated noise curves for Advanced LIGO (solid black line; Harry & the LIGO Scientific Collaboration 2010) and Advanced LIGO with optical squeezed light (dashed red line; H. Miao 2012, private communication). In this paper, we assume a low-frequency cutoff of 10 Hz. The features at 10 and a few hundred Hz are various thermal noise resonant modes of mirror suspensions. The modes at a few hundred Hz are suspension fiber resonances.

(A color version of this figure is available in the online journal.)

3.2. GW Parameter Estimation

Turning to GW parameter estimation, we summarize MCMC methods discussed in N10 and N11. Our central quantity of interest is the posterior density function (PDF) of the distribution of inferred source parameters, denoted by the vector of parameters $\boldsymbol{\theta}$, following a GW measurement. The PN inspiral waveform used in our work depends on the vector $\boldsymbol{\theta}$, which comprises the parameters $\{\mathcal{M}_z, \mu_z, D_L, \cos\theta, \phi, \cos\iota, \psi, t_c, \Phi_c\}$. Following Finn (1992) and Cutler & Flanagan (1994), we consider a data stream $s(t)$ measured at a detector a that comprises the instrument noise $n(t)$ and a GW signal $h(t, \hat{\boldsymbol{\theta}})$, where $\hat{\boldsymbol{\theta}}$ describes the source's "true" parameters, i.e., $s(t) = n(t) + h(t, \hat{\boldsymbol{\theta}})$. We assume that the noise at each detector has idealized Gaussian statistics. For a network of detectors, the PDF of the parameters $\boldsymbol{\theta}$ given some set of observed data streams $\boldsymbol{s}$ is

$$p(\boldsymbol{\theta}\,|\,\mathbf{s}) \propto p^{(0)}(\boldsymbol{\theta}) \mathcal{L}_{\rm TOT}(\mathbf{s}\,|\,\boldsymbol{\theta})\,, \tag{2}$$

where $\mathcal{L}_{\rm TOT}(\mathbf{s}\,|\,\boldsymbol{\theta})$ is the total likelihood function and $p^{(0)}(\boldsymbol{\theta})$ is the prior PDF that describes our prior knowledge of the signal's parameter distribution $\boldsymbol{\theta}$. The likelihood function measures the relative conditional probability of observing a particular data stream $\mathbf{s}$ given $\mathbf{h}$ and $\mathbf{n}$. By assuming that the noise is independent at each interferometer, the total likelihood function $\mathcal{L}_{\rm TOT}$ is equivalent to the product of the individual likelihoods at each detector. The likelihood $\mathcal{L}_a$ for detector a is given by (Finn 1992)

$$\mathcal{L}_a\,(s\,|\,\boldsymbol{\theta}) = e^{-(h_a(\boldsymbol{\theta}) - s_a\,|\,h_a(\boldsymbol{\theta}) - s_a)/2}\,. \tag{3}$$

The notation $(g|h)$ describes the noise-weighted cross-correlation of $g(t)$ with $h(t)$ in the vector space and is defined as

$$(g|h) = 2\int_0^\infty df\, \frac{\tilde{g}^*(f)\tilde{h}(f) + \tilde{g}(f)\tilde{h}^*(f)}{S_n(f)}, \tag{4}$$

where $S_n(f)$ denotes the instrument's power spectral density. We discuss the form of $S_n(f)$ in Section 3.3.

Using Equation (1), for an ensemble of detector noise realizations, the *expected* SNR at detector a is given by

$$\begin{aligned}\left(\frac{\mathrm{S}}{\mathrm{N}}\right)_{a,\mathrm{exp}} &= (h_a|h_a)^{1/2},\\ &= \sqrt{\frac{5}{96}}\frac{c}{D_L}\frac{2}{\pi^{2/3}}\left(\frac{G\mathcal{M}_z}{c^3}\right)^{5/6}\\ &\quad\times\left[F^2_{a,+}(1+\cos^2\iota)^2 + 4F^2_{a,\times}(\cos^2\iota)\right]^{1/2}\\ &\quad\times\left[\int_{f_{\mathrm{low}}}^{f_{\mathrm{ISCO}}}\frac{f^{-7/3}}{S_h(f)}df\right]^{1/2},\end{aligned} \tag{5}$$

where f_{low} is the instrument's low-frequency cutoff. Averaging over all possible binary sky positions and orientations, the expected sky-and-inclination-averaged SNR is given by (see Dalal et al. 2006)

$$\begin{aligned}\left(\frac{\mathrm{S}}{\mathrm{N}}\right)_{a,\text{sky-inc-ave}} &= \frac{8}{5}\sqrt{\frac{5}{96}}\frac{c}{D_L}\frac{1}{\pi^{2/3}}\left(\frac{G\mathcal{M}_z}{c^3}\right)^{5/6}\\ &\quad\times\left[\int_{f_{\mathrm{low}}}^{f_{\mathrm{ISCO}}}\frac{f^{-7/3}}{S_h(f)}df\right]^{1/2}.\end{aligned} \tag{6}$$

For a binary that is directly face-on to an observer ($\cos\iota = \pm1$), its $\mathrm{SNR}_{\mathrm{exp}}$ is a factor of $\sqrt{5/2} \simeq 1.58$ greater than its inclination-averaged counterpart $\mathrm{SNR}_{\text{inc-ave}}$ at the same position and distance, and a factor of $\sqrt{5/4} \simeq 1.12$ greater than its sky-and-inclination-averaged $\mathrm{SNR}_{\text{sky-inc-ave}}$ (see N10; Dalal et al. 2006). Throughout the rest of the paper, we use Equations (5) and (6) for GW-detectability (SNR-based) scaling arguments. We define the expected network SNR as the root-sum-square of the expected individual detector SNRs.

To infer the geometric source parameters for each NS binary considered, in particular the subset $(D_L, \cos\iota, \cos\theta, \phi)$, we map out the full posterior PDF of all source parameters using a Markov chain Monte Carlo (MCMC), given an observed data stream $\mathbf{s}_a$ at a detector. The Metropolis–Hastings MCMC algorithm used is based on a generic version of CosmoMC, described in Lewis & Bridle (2002). We assume prior distributions in all source parameters to be flat over the region of sample space where the binary is detectable at an expected network SNR = 3.5. For each MCMC simulation used on a single NS binary inspiral, we derive marginalized parameter measures and rms errors over $(D_L, \cos\iota, \cos\theta, \phi)$ at 68%, 95%, and 99% confidence regions (henceforth denoted as c.r.).

3.3. GW Networks

We consider GW networks consisting of combinations of LIGO (which comprises LIGO Hanford and LIGO Livingston), Virgo, LIGO India, and KAGRA. In the rest of the paper, we use the following notation to describe different GW networks with n detectors.

1. Net3 or network 3 is LIGO Hanford, LIGO Livingston, and Virgo;
2. Net4I or network 4I is LIGO Hanford, LIGO Livingston, Virgo, and LIGO India;
3. Net4K or network 4K is LIGO Hanford, LIGO Livingston, Virgo, and KAGRA;
4. Net5 or network 5 is LIGO Hanford, LIGO Livingston, Virgo, LIGO India, and KAGRA.

Apart from LIGO India, the detector's positions (as measured from Earth's center) used in this work are given in Table 1 of N10. For LIGO India's position and orientation, we use east longitude $\lambda = 76.7$, north latitude $\varphi = 14.3$, orientation $\upsilon = 0$, x-arm tilt $\Omega_x = 0$, and y-arm tilt $\Omega_y = 0$.

For simplicity, we assume that the noise sensitivity curve for each detector is represented by the anticipated broadband-tuned sensitivity curve for a single advanced LIGO detector, as shown in Figure 1. We impose a low-frequency cutoff at 10 Hz and frequencies below 10 Hz are not included in our analysis. In practice, LIGO, Virgo, and KAGRA will have different noise sensitivities in different frequency bands because of variations in each instrument's design. We also consider the anticipated sensitivity curve for LIGO Livingston and LIGO Hanford interferometers using optically squeezed light (H. Miao 2012, private communication). To compare different GW network abilities, for each NS–NS or NS–BH binary, we assign a unique noise realization to each GW detector, which we keep constant when adding and subtracting detectors to a network. In addition, we assume that each GW interferometer operates at an idealized 100% of the time (see Schutz 2011 for estimates of different instruments' duty cycles).

3.4. GW Triggering Criteria

For each binary in the two catalogs, we implement three GW triggering scenarios that use the following

1. A coincident trigger criterion (denoted by "a"): we select the binary if at least two GW detectors each have an SNR > 6 and if the expected network SNR > 12. The estimated number of required and desired false-alarm rates for GW templates determines the choice in particular SNR threshold values (Owen 1996 and see e.g., N11; Abadie et al. 2012a).
2. A coherent trigger criterion (denoted by "b"): we select the binary if its GW expected network SNR > 8.5 (see, e.g., N11; Harry & Fairhurst 2011).
3. An EM-precursor coherent trigger criterion: we select the binary if its GW expected network SNR > 7.5. Henceforth, to avoid confusion with the coherent trigger above, we refer to this case as an EM-precursor trigger criterion. As discussed in N10, we choose to lower the network threshold in the presence of an already observed EM counterpart because prior knowledge of the merger time and sky position reduces the number of searched GW templates. Models of EM-precursor emission to NS binary mergers include resonant shattering of NS crusts observable in γ- and X-rays (e.g., Tsang et al. 2012) and a coherent burst of radio emission produced by magnetically dominated outflows (Pshirkov & Postnov 2010; Piro 2012).

For all scenarios, the interferometers may have significantly non-Gaussian noise, necessitating an increase in the SNR threshold to take into account complex detector statistics.

4. GW-DETECTED BINARY POPULATIONS: RESULTS

This section presents the *relative* fraction, rates, and distributions of geometric parameters of NS–NS or NS–BH

Table 1
Relative Fractions $\times 10^{-4}$ of NS–NS and NS–5-$M_{\odot}$-BH Mergers with Collimated (Denoted as "B") and Isotropic (Denoted as "I") Emission Detectable in GWs Using Three Different Selection Criteria with Four GW Networks

GW Network		Net3 $\mathrm{B}\mid\mathrm{I}$	Net4I $\mathrm{B}\mid\mathrm{I}$	Net4K $\mathrm{B}\mid\mathrm{I}$	Net5 $\mathrm{B}\mid\mathrm{I}$
Coincident *"a"*	NS–NS	$0.3 \pm 0.3 \mid 11 \pm 2$	$0.3 \pm 0.3 \mid 17 \pm 2$	$0.3 \pm 0.3 \mid 17 \pm 2$	$0.3 \pm 0.3 \mid 23 \pm 2$
	NS–5-$M_{\odot}$-BH	$0.7 \pm 0.5 \mid 50 \pm 4$	$1.0 \pm 0.6 \mid 79 \pm 5$	$1.3 \pm 0.7 \mid 77 \pm 4$	$2.3 \pm 0.9 \mid 104 \pm 6$
Coherent *"b"*	NS—NS	$0.8 \pm 0.4 \mid 36 \pm 3$	$0.8 \pm 0.4 \mid 57 \pm 4$	$0.8 \pm 0.4 \mid 59 \pm 4$	$1.5 \pm 0.6 \mid 78 \pm 4$
	NS–5-$M_{\odot}$-BH	$2.3 \pm 0.9 \mid 170 \pm 7$	$3.7 \pm 1.1 \mid 251 \pm 9$	$4.0 \pm 1.2 \mid 243 \pm 9$	$4.7 \pm 1.2 \mid 323 \pm 10$
EM precursor	NS–NS	$0.8 \pm 0.4 \mid 54 \pm 4$	$1.0 \pm 0.5 \mid 80 \pm 4$	$1.8 \pm 0.6 \mid 81 \pm 4$	$2.0 \pm 0.7 \mid 113 \pm 5$
	NS–5-$M_{\odot}$-BH	$3.0 \pm 1.0 \mid 244 \pm 9$	$4.0 \pm 1.2 \mid 350 \pm 11$	$4.3 \pm 1.2 \mid 350 \pm 11$	$6.3 \pm 1.5 \mid 464 \pm 12$
Coincident *"a"* + O.S.	NS–NS	$2.0 \pm 0.8 \mid 129 \pm 7$	$2.0 \pm 0.8 \mid 140 \pm 7$	$2.0 \pm 0.8 \mid 140 \pm 7$	$2.3 \pm 0.9 \mid 152 \pm 7$
	NS–5-$M_{\odot}$-BH	$6.7 \pm 1.5 \mid 490 \pm 12$	$8.0 \pm 1.6 \mid 535 \pm 13$	$8.7 \pm 1.7 \mid 534 \pm 13$	$9.3 \pm 1.7 \mid 579 \pm 13$
Coherent *"b"* + O.S.	NS–NS	$4.7 \pm 1.2 \mid 364 \pm 11$	$4.7 \pm 1.2 \mid 391 \pm 11$	$4.7 \pm 1.2 \mid 390 \pm 11$	$5.0 \pm 1.3 \mid 418 \pm 12$
	NS–5-$M_{\odot}$-BH	$27.7 \pm 3.0 \mid 1517 \pm 21$	$30.0 \pm 3.2 \mid 1643 \pm 21$	$30.7 \pm 3.2 \mid 1640 \pm 21$	$33.0 \pm 3.3 \mid 1777 \pm 22$
EM precursor + O.S.	NS–NS	$8.0 \pm 1.6 \mid 517 \pm 13$	$9.0 \pm 1.7 \mid 565 \pm 13$	$9.3 \pm 1.8 \mid 557 \pm 13$	$10.0 \pm 1.8 \mid 610 \pm 14$
	NS–5-$M_{\odot}$-BH	$33.0 \pm 3.3 \mid 2062 \pm 23$	$36.0 \pm 3.4 \mid 2248 \pm 24$	$37.0 \pm 3.5 \mid 2246 \pm 24$	$39.3 \pm 3.6 \mid 2425 \pm 25$

Notes. The notation "OS" represents optical squeezing in the LIGO interferometers. The range given represents the 1σ statistical error of our simulation.

inspirals detected by different GW networks of interferometers. We define relative fraction as the ratio of GW-detected binary mergers out of the total number of binaries in each catalog.

4.1. Relative Fractions of GW-detected Events

For each NS binary merger in our two catalogs, we compute and compare GW SNRs to a defined threshold SNR at a particular detector or at a network (Section 3.4). For different progenitors, GW networks, and triggering criteria, we thus obtain fractions of those mergers that are detectable by GWs out of the catalog's total number of systems. Table 1 shows relative fractions of GW-detected merger samples.

Table 1 also indicates the relative fraction of GW-detected mergers that have their orbital angular momentum vectors oriented toward the Earth such that they could show collimated γ- and X-ray emission. Observations exist for two SGRBs indicating a half-jet opening angle θ_{j} of $\sim 7°$ (Burrows et al. 2006; Soderberg et al. 2006) and $\sim 3°$–$8°$ (Fong et al. 2012). A handful of other SGRBs exhibit upper- and lower-bound jet-break measurements, discussed in Section 5.1. In this work, we define beamed binaries as those binaries whose orbital angular momentum vector lies within a relatively stringent θ_{j} of $6°$.

Table 1 illustrates several trends between different samples of GW-detected NS binary mergers. Schutz (2011) provides powerful analytically derived expressions that show good agreement with our explicit results. First, the fraction f_{beamed} of beamed NS binary mergers seen in GWs, observable from all possible inclination angles ι, is less than those binaries with isotropic orientation (see Schutz 2011; Metzger & Berger 2012). When $\iota \ll \theta_{\mathrm{j}}$, $f_{\mathrm{beamed}} \sim 1 - \cos\theta_{\mathrm{j}} \sim \theta_{\mathrm{j}}^{2}/2$ for small θ_{j}; in our case, the empirically derived range $f_{\mathrm{beamed}} \sim 0.5\%$–$1\%$ agrees well with its theoretical value of 0.7%. Second, the relative fraction of GW-detected NS–5-$M_{\odot}$-BH mergers is greater than GW-detected NS–NS mergers by a factor of four to five. This follows from Equation (6), where SNR scales as $\mathcal{M}_c^{5/6}$ and detectable volume thus scales as $\mathcal{M}_c^{15/6}$. For our NS–NS and NS–5-$M_{\odot}$-BH inspirals, values for $\mathcal{M}_c$ are 1.21 $M_{\odot}$ and 2.22 $M_{\odot}$, respectively. Third, the fractions of GW-detected events where the two LIGO interferometers use squeezed light are a factor of ~ 9 to 10 greater than for those networks where no optical squeezing is implemented. Illustrated in Figure 1, the optically squeezed advanced LIGO noise curve is a factor of two to three more sensitive than the standard analog's curve. From Equation (6), such an improvement in instrument sensitivity translates to an improvement by a factor of $\sim 2^3$–3^3 in detectable volume (because SNR is inversely proportional to D_L). Fourth, increasing the number of GW detectors in a network from 3 to 5 increases the number of GW-detected mergers by a factor of ~ 2 or less (see N10). Shown in Equation (6), the network $\mathrm{SNR}_{\mathrm{exp}}$ scales as $\sim\sqrt{n}$, where n is the number of detectors.

4.2. Estimated Relative Rates of GW-detected Inspirals

To convert relative GW-detected fractions into relative GW-detected rate predictions, we first require estimates of the astrophysical NS binary merger rate, independent of GW detection. In the case of NS–NS binaries, different astrophysical merger rates are derived either by extrapolating the distribution of observed Galactic binary pulsars or from population synthesis results (see, e.g., Phinney 1991 and references in Abadie et al. 2010). The rates range from 0.01 to 10 $\mathrm{Mpc}^{-3}\,\mathrm{Myr}^{-1}$, with 1 $\mathrm{Mpc}^{-3}\,\mathrm{Myr}^{-1}$ being the mean of the rate's PDF (Abadie et al. 2010). In contrast, because we have yet to observe a NS–BH system, all estimates of NS–BH merger rates are based entirely on theoretical population synthesis results. The rates range from 6×10^{-4} to 1 $\mathrm{Mpc}^{-3}\,\mathrm{Myr}^{-1}$, where 0.03 $\mathrm{Mpc}^{-3}\,\mathrm{Myr}^{-1}$ is defined as a realistic rate in Abadie et al. (2010). Therefore, our estimates for GW-detected merger rates rely on theoretical

Table 2

Representative GW Network Scenarios for Detectable Samples of NS–NS and NS–BH Mergers

Feature	Lower-bound Scenario	Upper-bound Scenario
Relative fractions and rates	Coincident 3 detector: Net3a 19 yr^{-1} (NS–NS) | 3 yr^{-1} (NS–BH)	Coherent 5 detector: Net5b 138 yr^{-1} (NS–NS) | 17 yr^{-1} (NS–BH)
Detectable distance	Coincident 3 detector: Net3a 220–400 Mpc (med-max; NS–NS) 350–600 Mpc (med-max; NS–BH)	Coherent 5 detector:Net5b 390–750 Mpc (med-max; NS–NS) 650–1250 Mpc (med-max; NS–BH)
Sky area errors	Coherent 3 detector: Net3b 55–180 deg^2 (med-max; NS–NS) 50–170 deg^2 (med-max; NS–BH)	Coincident 5 detector: Net5a 7–120 deg^2 (med-max; NS–NS) 6–65 deg^2 (med-max; NS–BH)

Note. The notations med. and max. refer to the median and maximum values of parameter distributions.

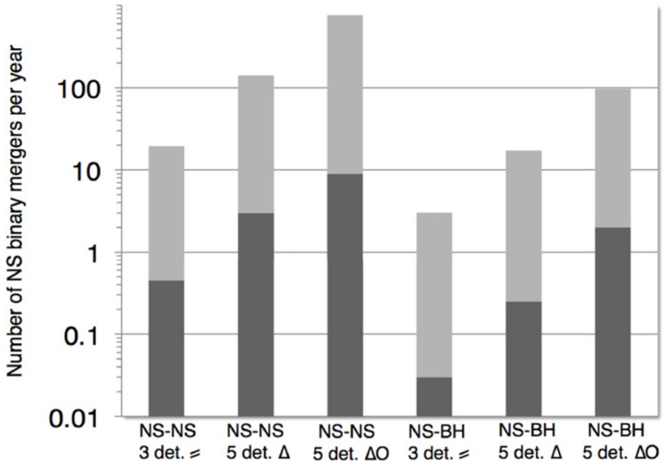

Figure 2. Relative rate of NS binary mergers detected by different GW networks and triggering criteria. The dark gray shaded regions denote those binaries that have their orbital angular momentum vector lying within a half-jet opening angle of 6° and the light gray shaded regions denote those binaries whose orbital angular momentum have half-jet opening angle greater than 6°. The notation 3 det. ⫽ refers to Net3a, a coincident-triggered network 3, 5 det. Δ denotes Net5b, a coherent-triggered network 5, and 5 det. Δ◯ represents a Net5b with optical squeezing in the two LIGO interferometers.

predictions of NS binary merger rates that span three orders of magnitude.

Here, we estimate $\mathcal{R}_{\text{NS-X}}$, NS binary merger rates detected by networks of GW interferometers, using

$$\mathcal{R}_{\text{NS-X}} = \mathcal{N}_{\text{NS-X}} \times f_{\text{NS-X}} \times V \times \frac{1}{k}, \tag{7}$$

where the subscript X denotes a NS or BH, and $\mathcal{N}_{\text{NS–NS}}$ and $\mathcal{N}_{\text{NS–BH}}$ are the astrophysical NS–NS and NS–5-$M_\odot$-BH merger rates in $\mathrm{Mpc}^{-3}\ \mathrm{yr}^{-1}$, respectively. V is the total volume that the catalogs encompass (in our case, this corresponds to $\sim 4/3 \times \pi \times (2.82\,\mathrm{Gpc})^3$) and $f_{\text{NS-X}}$ are the relative fractions of GW-detected NS binary mergers. Table 1 gives values of $f_{\text{NS-X}}$ for different progenitors, GW networks, and triggering criteria. The factor $k \sim 3\sqrt{3}$ applies to all networks with any number of detectors. It incorporates the Abadie et al. (2010) correction for the GW interferometers' non-stationary and non-Gaussian noise, applied in order to achieve required false-alarm rates.

Figure 2 shows relative rates of GW-detected NS binary mergers which have either isotropic or beamed emission. We use the mean and/or realistic rate of NS binary mergers quoted in Abadie et al. (2010). Given the few orders-of-magnitude uncertainty, we use NS–10-$M_\odot$-BH merger rates as representative for the merger rates of NS–5-$M_\odot$-BH systems used in this work. For NS–NS mergers, we use a value of ∼18,270 for the prefactor [$\mathcal{N}_{\text{NS-X}}\,(V/k)$] in Equation (7). For NS–BH mergers, we use a value of ∼550 for the prefactor [$\mathcal{N}_{\text{NS-BH}}\,(V/k)$]. Let us now discuss several features of Figure 2.

First, out of all possible GW networks and triggering schemas, we present relative NS–NS and NS–BH binary merger rates detected by GWs under three scenarios.

1. Net3a: coincident-triggered network 3;
2. Net5b: coherent-triggered network 5;
3. Net5b with optically squeezed LIGO.

Due to the high SNR threshold required at two detectors or more, Net3a detects the fewest number of NS–NS or NS–BH mergers. It provides a lower bound on the number of detected GW events, indicative of how the early years of GW measurements might unfold. In contrast, Net5b detects the largest number of mergers of NS–NS or NS–BH mergers, because the coherent-network SNR scales as $\sqrt{n}$, where $n = 5$ is the maximum number of detectors. It hence provides an upper bound on the number of GW-detected mergers, suggestive of how a GW network might operate after the first several years of GW measurements. The third scenario, envisioned later in the timeline of the development of the GW network, provides a highly optimistic bound for NS–NS and NS–BH mergers detected using Net5b with optically squeezed LIGO; we choose to investigate this scenario in a future study. Summarized in Table 2, we use Net3a and Net5b to indicate representative bounds for the performance between different GW networks and triggering schema. Illustrated by Figure 2, our GW-detected NS binary merger rate estimates show good agreement with earlier works (e.g., Abadie et al. 2010). Differences occur because of different triggering criteria invoked and SNR thresholds used.

Second, the dark gray shaded regions in Figure 2 denote those binaries that have their orbital angular momentum vector lying within a relatively stringent $\theta_{\mathrm{j}} < 6°$ and the light gray shaded regions denote those binaries whose orbital angular momentum have $\theta_{\mathrm{j}} > 6°$. From one to several NS binary mergers per year could have $\theta_{\mathrm{j}} < 6°$ and may exhibit γ-ray collimation associated with SGRBs. Our beamed NS–NS binary merger rates are consistent with SGRB rates of $10\,\mathrm{Gpc}^{-3}\ \mathrm{yr}^{-1}$, discussed in Metzger & Berger (2012), Coward et al. (2012), Enrico Petrillo & Dietz (2012), and Chen & Holz (2012).

Third, we emphasize that lower and upper bounds to the rate estimates differ, for instance, for NS–NS mergers by two orders of magnitude below and an order of magnitude above the mean values that we use. Results presented in Figure 2 are instructive in that they illustrate relative GW detectability rates between different GW networks and triggering criteria, but the values given here should be used with caution.

4.3. GW Malmquist Effect in Detected Events' Distances and Inclination Angles

GW detection criteria set implicit prior distributions on geometric parameters of NS binary mergers (see N10; Schutz 2011). Defined here as the GW Malmquist effect, our GW detection criterion preferentially selects for more face-on (or equivalently beamed and more "GW-luminous" binary inspirals); see Equation (5). The GW Malmquist bias is analogous to the standard Malmquist effect in observational astronomy, where intrinsically brighter objects are detected farther out. In GWs, beamed ($\cos\iota \rightarrow \pm 1$) binaries have higher SNRs and are intrinsically more luminous (Equation (5)).

Figure 3(a) shows the 2D distribution for parameters (D_L, $\cos\iota$) of NS–NS mergers detected in GWs with Net3a. Important for EM follow-up and for coincident EM and GW observations, we remark on noteworthy features of the distribution. Figure 3(a) illustrates the GW Malmquist bias toward detection of beamed binaries, with $\cos\iota \rightarrow \pm 1$. The distribution exhibits a characteristic V-shape which is consistent with the analytically derived PDF of detected values in ι given in Equation (28) of Schutz (2011). Unsurprisingly, we detect the majority of events at threshold and observe a paucity of close-in binaries, detected with distances less than 100 Mpc. The maximum distance for NS binary mergers detectable by Net3a is ∼400 Mpc. We note that the closest SGRBs with known redshifts are 080905, 050709, and 050724 at $z = 0.122$ (∼560 Mpc), $z = 0.161$ (∼760 Mpc), and $z = 0.257$ (∼1.28 Gpc); see Berger (2010). Therefore, the maximum detectable distance range of Net3a does not include the distances of the three closest SGRBs observed so far. Discussed in Metzger & Berger (2012), the lack of SGRBs observed within a few hundred megaparsecs is consistent with the *Swift* satellite's observational biases: only ∼1/10 of the sky is surveyed at a particular epoch and only ∼1/3 of SGRBs observed by *Swift* have redshifts. Finally, in Figure 3(b), we show the 2D distribution of NS–NS mergers for the parameters (D_L, $\cos\iota$) detected by Net5b. We note that the maximum detectable distance increases by a factor of 1.5 compared to Net3a. Moreover, in the case of our NS–5-$M_\odot$-BH catalogs, the SNR and hence detectable distance depends on the chirp mass $\mathcal{M}_c^{5/6}$ (Equation (6)). Therefore, the maximum detectable distance increases to above 1 Gpc in Figure 3(c).

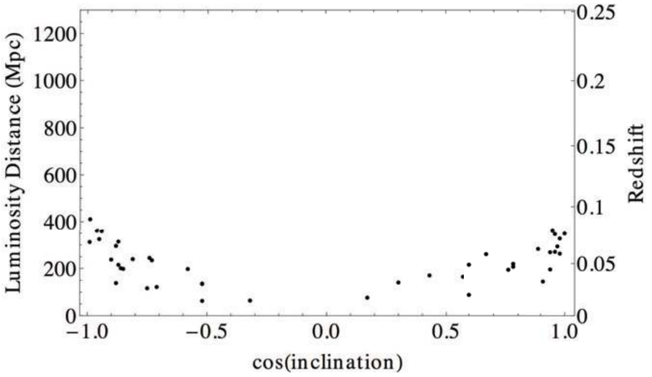

(a) NS-NS mergers detected in GWs by Net3a

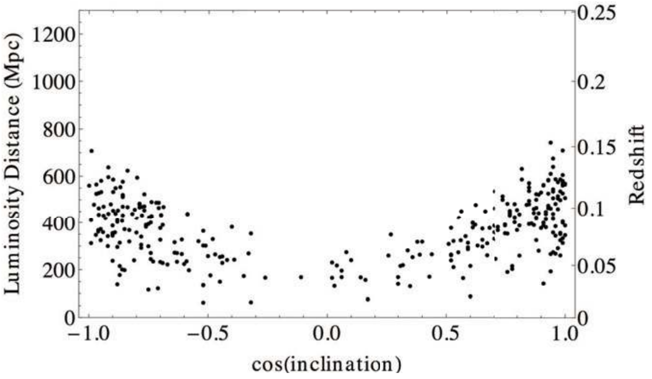

(b) NS-NS mergers detected in GWs by Net5b

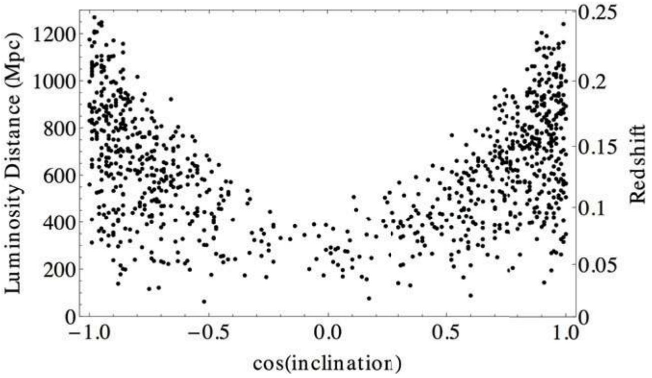

(c) NS-BH mergers detected in GWs by Net5b

Figure 3. 2D marginalized prior distribution in D_L and $\cos\iota$ for GW-detected NS binary mergers. Each point represents a GW-detected NS binary merger. The top panel shows NS–NS mergers detected by Net3a. The middle panel shows NS–NS mergers detected by Net5b. The bottom panel shows NS–BH mergers detected by Net5b. Redshifts are computed assuming cosmological parameters given in Komatsu et al. (2009).

4.4. Cumulative Distribution of GW Distances and Localization Errors

Critical for EM follow-up, we examine cumulative distributions in GW distance and sky area errors for populations of NS–NS and NS–BH inspirals detected using different GW detector networks and triggering criteria. For representative populations of GW-detected NS binary mergers, we randomly take 200 NS–NS and 200 NS–BH inspirals from their maximum sample detected in GWs with Net5b. We assume standard advanced LIGO-like noise curves with no optically squeezed light.

Figures 4(a) and (b) show the *specific* distribution in luminosity distance (in Mpc) of NS–NS and NS–BH mergers detected by different GW networks and triggering schema. We use the term specific because we normalize the cumulative distribution to the sample of NS binary mergers that a particular triggered GW network can detect. Shown in Table 2, similar to Section 4.1, Net3a and Net5b provide the representative lower and upper bounds of the GW detectable distance. For NS–NS mergers, we find that median detectable distances are 180 Mpc and 370 Mpc with Net3a and Net5b, respectively. For NS–BH mergers, we find that the median detectable distances are 240 Mpc and 660 Mpc with Net3a and Net5b, respectively.

Illustrated in Figures 4(a) and (b), two distinct distributions for detectable distance exist depending on whether the GW trigger is coincident versus coherent. In contrast, we find that detectable distance ranges depend only weakly on the number of detectors in a network. From Figure 4(b), the detectable distance ranges for NS–BH mergers are approximately a factor of two greater than for NS–NS mergers (see Equation (6), Sections 4.1 and 4.3).

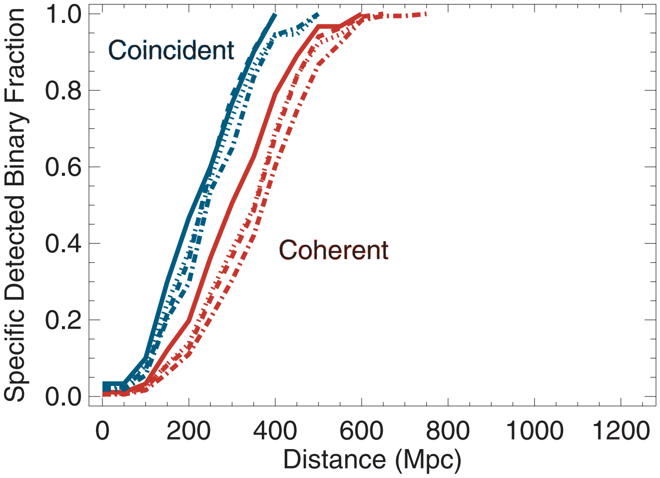

(a) NS-NS binary mergers

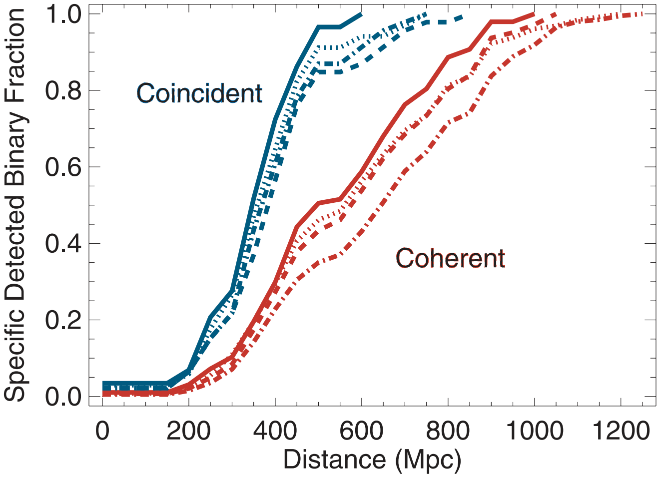

(b) NS-BH binary mergers

Figure 4. Cumulative luminosity distance (in Mpc) distribution of the detected sample of NS–NS (top panel) and NS–BH (bottom panel) mergers normalized to each specific network and trigger criterion. The blue lines denote those NS mergers detected using a coincident-trigger criterion; the red lines represent those events detected using the GW network coherently. Solid lines represent GW network 3, dotted lines denote GW network 4I, dashed lines are GW network 4K, and dash-dotted lines are GW network 5.

(A color version of this figure is available in the online journal.)

In addition to distance, EM follow-up detectability relies on sky area error ranges; see Figures 5(a) and (b) and Section 5. From Figures 5(a) and (b),[8] we find that a coherent-triggered network 3 provides the largest sky area errors for GW mergers. We refer to this scenario as Net3b and it represents our "lowest bound" on sky area errors (Table 2). On the other hand, a coincident-triggered network 5, denoted as Net5a, provides the smallest sky area errors and represents our "upper bound" for sky localization (Table 2).

From Figures 5(a) and (b), we find that 50% of NS–NS mergers are detected to within 7 deg^2 with Net5a and to within 60 deg^2 with Net3b. For NS–BH mergers, we find that 50% of events are detected to within 6 deg^2 with Net5a and to within 55 deg^2 using Net3b. As expected, similar distributions in sky area error exists between GW-detected NS–NS and NS–BH merger populations because most events are detected at threshold SNR.

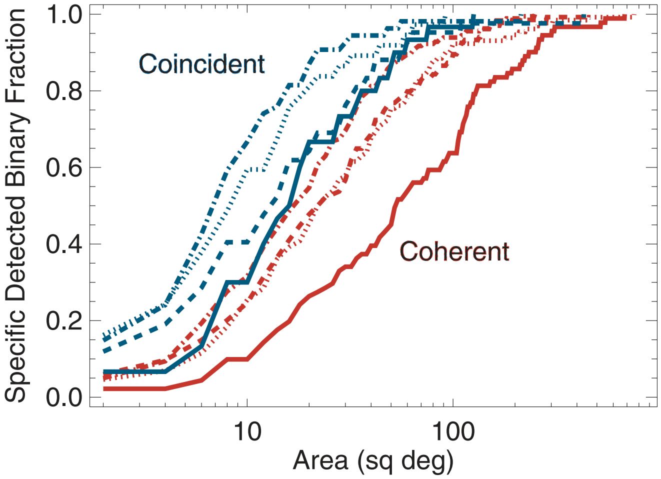

(a) NS-NS binary mergers

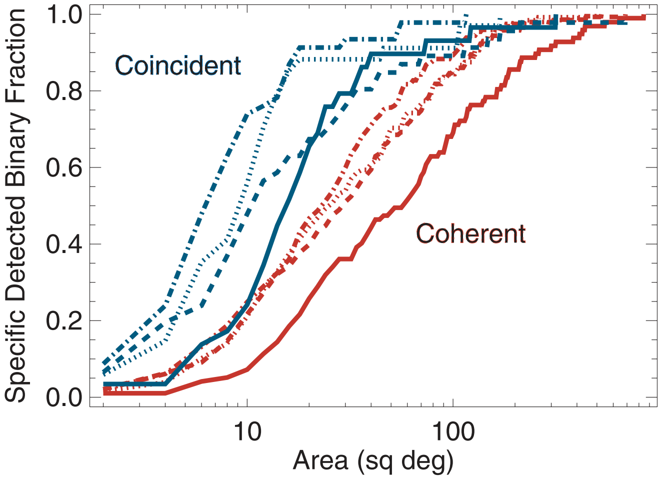

(b) NS-BH binary mergers

Figure 5. Cumulative sky error (in deg^2 at 95% c.r.) distributions of the detected sample of NS–NS mergers normalized to each specific network and trigger criterion. The blue lines denote those NS–NS (top panel) and NS–BH (bottom panel) mergers detected using a coincident-trigger criterion; the red lines represent those events detected using the GW network coherently. Solid lines represent GW network 3, dotted lines denote GW network 4I, dashed lines are GW network 4K, and dash-dotted lines are GW network 5.

(A color version of this figure is available in the online journal.)

We find elliptically shaped sky errors for the majority of our examined NS binary mergers (see Section 6.1 for an example); differing GW arrival times at each detector dominate sky area reconstruction rather than parameter degeneracies in the GW waveform's antenna functions (see N11). In a handful of cases, we find multimodal peaks for especially weak SNR events because of larger uncertainties in arrival times at detectors. In addition, we find that sources located in (or close-by to) the degenerate Net3 plane have relatively poor angular resolution (see also Fairhurst 2011; Wen & Chen 2010; N11; Veitch et al. 2012). An improvement by a factor of two in the normalized cumulative sky error is seen with network 4I (LIGO+Virgo with LIGO India) compared to network 4K (LIGO+Virgo with KAGRA) only in the case of using a coincident trigger. Given that LIGO

---

[8] In contrast, Figures 3 and 4 in N11 show sky error distributions for subsets of NS binary mergers detected by different GW networks that are normalized to the full detected sample by network 5. In this work, instead of emphasizing the reduced number of detections, we particularly wish to answer what percentage of NS binary mergers are detected by a known triggered network to a certain sky area error.

India is located farther away from the degenerate LIGO–Virgo plane than KAGRA, such a factor of two improvement in sky area error is expected (e.g., Schutz 2011).

4.5. GW Volume Estimates

Measurements by GW networks provide us with distance and sky area errors. With both values in hand, we can construct GW volumes, which aid in identifying the EM counterparts of NS binary mergers (as Section 6.2 describes in detail).

As a first attempt, we introduce and define below the term low-latency GW volumes. Such volumes in principle can be computed within a few to tens of minutes of a GW detection (and do not rely on the full MCMC machinery used in this work); hence they are critical for EM follow-up. In their final science run before halting for upgrades to their advanced versions, LIGO and Virgo sent triggers to EM telescopes within ∼30 minutes of a possible GW signal being detected (LIGO Scientific Collaboration et al. 2012a; Abadie et al. 2012b; Evans et al. 2012); most of this time was spent for human-limited verification checks at each detector site. In the era of advanced detectors, efforts are underway to reduce the latency timescale to less than 10 minutes (Singer et al. 2012; Cannon et al. 2012).

In this work, we compute low-latency GW volumes by using only marginalized 2D sky area errors and marginalized 1D distance measures (all at 95% c.r.). As we now discuss, although in this work we derive sky area and distance errors by marginalizing the full 9D PDF, we could instead have used computations of approximate sky area errors and distance measures on time-scales of ∼ minutes. Regarding sky localization errors for the majority of GW-detected mergers, analytically derived formulae (e.g., Wen & Chen 2010; Fairhurst 2011), computed on timescales of seconds, allow for sky reconstruction estimates that are in good agreement with explicitly derived 2D sky errors presented in N11. This is because different GW arrival times at each detector dominate over amplitude corrections in the GW waveform. Regarding distance measures, Fisher matrix-based estimates allow for rough distance measures on a timescale of seconds (see, e.g., Ajith & Bose 2009). In practice, however, measured distances for the majority of threshold events will have significantly larger errors (by a factor of several) from their Fisher-matrix-derived counterparts (N10). This is because degeneracies between the sources' geometric parameters that appear in the GW waveforms' amplitude inhibit measurement inference for low SNR events (see N10 for a detailed discussion). Therefore, a possible solution when estimating low-latency distance measures is to use their Fisher-matrix-derived errors multiplied by a factor of three (see N10; Del Pozzo 2012).

To compute low-latency GW volumes, we use upper, mean, and lower distance measures; we define d_u and d_l to be the upper and lower 1D marginalized distance values at 95% c.r. We replace d_u with d_h the horizon or maximum detectable distance of a coincident- or coherent-triggered GW network when $d_u > d_h$. We show absolute volumes in Mpc^3 as a function of the mean distance with their upper and lower distance errors for NS–NS and NS–BH mergers detected by Net3a and Net5b, respectively (Figures 6(a) and (b)). As expected, the GW measured upper and lower distance ranges are noticeably smaller for those NS–NS and NS–BH binaries with true distances less than 200 and 500 Mpc, respectively.

5. EM DETECTABILITY

In this section, we first review characteristics of suggested EM counterparts to compact binary mergers. We then discuss EM detectability by upcoming or current optical and infrared telescopes.

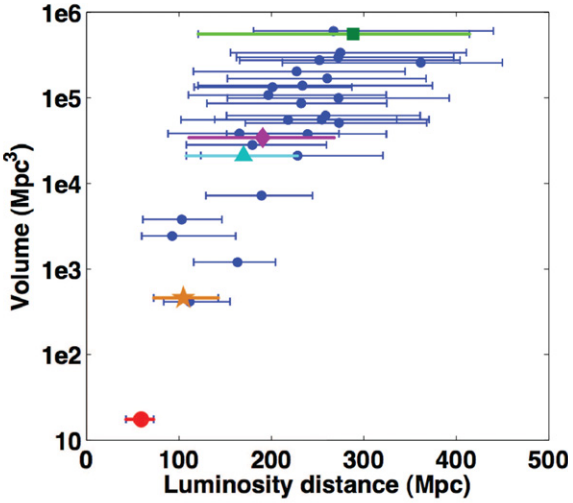

(a) NS-NS binary mergers observed by GW Net3a

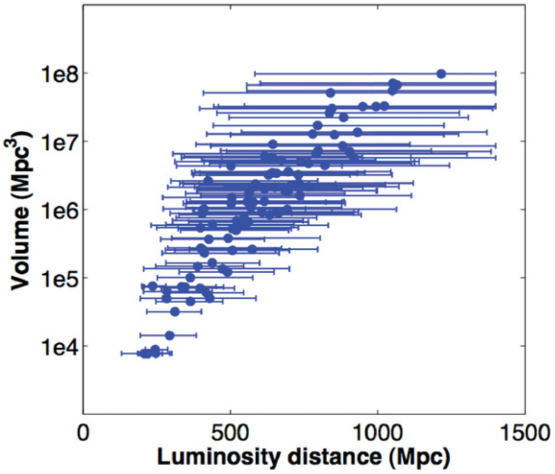

(b) NS-BH binary mergers observed by GW Net5b

Figure 6. Absolute measures in volume (Mpc^3) for a detected sample of NS–NS mergers observed by GW Net3a (top panel) and NS–BH mergers observed by GW Net5b (bottom panel). Each filled point represents a detected NS binary merger at its mean luminosity distance. The horizontal error bars represent the upper and lower 1D marginalized distance values at 95% c.r. for each NS binary merger. The different colors represent different case studies of NS–NS mergers examined in Section 6.1: green is Case I (beamed binary), red is Case II (a nearby binary), light blue is Case III (a merger at low Galactic latitude), purple is Case IV (a merger at high Galactic latitude), and orange is Case V (a binary in a dense galaxy cluster environment). Specifically, the green square is Case I, the red circle is Case II, the light blue triangle is Case III, the purple diamond is Case IV, and the orange star is Case V.

(A color version of this figure is available in the online journal.)

5.1. Predicted EM Counterparts to NS Binary Mergers

Short gamma-ray bursts (SGRBs). The leading progenitor models for the majority of observed SGRBs are NS–NS and NS–BH mergers (see, e.g., Eichler et al. 1989; Paczynski 1991; Narayan et al. 1992). The hypothesis has been further supported by around 40 SGRB observations triggered by the *Swift* satellite and followed-up by rapid multiwavelength observations (e.g., Berger et al. 2005; Fox et al. 2005; Hjorth et al. 2005; Bloom et al. 2006; Berger 2011). Theoretical models assume that accretion by a rotationally supported disk onto a newly formed BH (or rapidly rotating NS) powers a relativistically collimated outflow, which results in the observed prompt gamma-ray emission (e.g., Ruffert et al. 1997; Rosswog et al. 2003; Shibata & Taniguchi 2008; Rezzolla et al. 2011). Due to their high Lorentz factors and energies, the prompt γ-ray emission is assumed to be relativistically beamed with initial gamma-ray emission that lasts for $<2s$ (hence the use of the name "short" when classifying SGRBs; see Nakar 2007 for a review). Jet-break observations in at least two SGRBs suggest collimation of half opening angles of $\sim 7^\circ$ (Soderberg et al. 2006; Burrows et al. 2006) and 3°–8° (Fong et al. 2012), respectively. Upper and lower limits exist in a few other cases (e.g., Fox et al. 2005; Grupe et al. 2006). As the relativistic beamed outflow interacts with the surrounding medium, we expect to observe afterglow signatures in the X-ray and optical occurring at longer timescales from minutes to days. Observations of EM afterglows suggest energies of $E \lesssim 10^{51}$ erg and circumburst densities of $n \lesssim 0.1\,\mathrm{cm}^{-3}$ (Berger et al. 2005; Soderberg et al. 2006). Afterglow model predictions as a function of E and n are given in van Eerten & MacFadyen (2011) and van Eerten et al. (2012).

R-process radioactivity transients–kilonova. Initially proposed by Li & Paczyński (1998), rapid (r)-process radioactivity-powered transients are weak supernovae-like events. In this paper, we refer to such transients as "kilonovae," so-called because their predicted peak luminosities are estimated to be a factor $\sim 10^3$ greater than standard novae (Kulkarni 2005; Metzger et al. 2010; Roberts et al. 2011). A central premise of the model is that NS mergers produce ejecta from either dynamically ejected tidal tails or accretion disk outflows driven by early neutrino winds or late thermonuclear-driven winds (e.g., Kulkarni 2005; Metzger et al. 2008, 2009; Dessart et al. 2009). The ejecta is gravitationally unbound and does not fall back onto the newly formed BH or rapidly rotating NS. Numerical relativity and smoothed particle hydrodynamic simulations predict a two orders of magnitude difference in the mass of the ejecta (0.001–0.1 $M_\odot$) and a factor of a few difference in the ejecta's velocity (0.1–0.3 c); see, e.g., Rosswog et al. (1999), Rantsiou et al. (2008), Foucart et al. (2011), Piran et al. (2013), East & Pretorius (2012), and East et al. (2012). Following the expansion of neutron-rich material from nuclear densities, r-process nucleosynthesis produces heavier unstable radioactive elements which subsequently beta-decay and fission back to stability on longer timescales. We expect the material to act as a heat source and the subsequent emission to radiate isotropically. Based on highly uncertain opacities, light curves and color evolutions using radiative transfer models suggest that the emission peaks either in the optical or near-infrared. In the optical, the emission could peak with luminosities of 10^{41}–$10^{42}\,\mathrm{erg\,s^{-1}}$ which decay on half- to five-day timescales (Metzger et al. 2010). Peak absolute magnitudes M_R range from -14 to -17 mag and depend on the assumed ejecta mass, velocity, opacity calculations, and nuclear reactions (Metzger & Berger 2012). On the other hand, preliminary work estimates peak absolute magnitudes of $M_H = -15.5$ mag in the near-infrared ($\sim 1.7\,\mu$m) assuming an ejecta mass of 0.01 $M_\odot$ at $0.1c$ with timescales varying from several to tens of days (Barnes & Kasen 2013). Efforts are currently underway to predict the spectroscopic Doppler-broadened signature of kilonovae.

Radio counterparts. There are three predicted radio counterparts: (1) we expect observable non-thermal radio emission from beamed ultrarelativistic ejecta of SGRBs (Berger et al. 2005; Soderberg et al. 2006; Chandra & Frail 2012), (2) we could observe a coherent radio burst emitted from a magnetically driven, relativistic plasma outflow prior to the NS merger (Hansen & Lyutikov 2001; Pshirkov & Postnov 2010), and (3) recent work suggests incoherent radio signatures from blast waves produced by the interaction of quasi-spherical, sub-relativistic or mildly relativistic ejecta with the interstellar medium (Nakar & Piran 2011). Nakar & Piran (2011) estimate that radio flares may peak at 1.4 GHz emission for weeks out to redshifts of 0.1 ($\sim$450 Mpc) and can be detectable at milliJansky levels. If the outflows are sub-relativistic, flares may be detectable on a timescale of year at 150 Mpc at closer distances with current and near-future surveys.

5.2. *Differences between EM Counterparts*

We highlight four features that distinguish the proposed EM counterparts and help define search strategies. First, the counterparts exhibit either beamed or isotropic emission. SGRBs have collimated jet emission and only accompany a very small fraction of NS–NS and NS–BH mergers (Table 1). On the other hand, kilonovae and radio remnants have predicted isotropic emission and accompany *all* NS–NS and NS–BH mergers. Second, there is a wide disparity in timescales for fast and slow counterparts. SGRBs last for seconds (and their afterglows decay as a power law in time), kilonovae last for hours to days and radio transients, last for months to years. Third, the rate of false positives is considerably different across EM wavelengths. The precise timing of the SGRB overcomes the challenge of poor sky localization of GW events. The quietness of the transient radio sky is a boon to the small number of spatially coincident false positives (Frail et al. 2012). The dynamic optical sky results in tens to hundreds of false positives that would be spatially and temporally coincident with GW events and search strategies are necessary to separate the wheat from the chaff. Fourth, discovery and follow-up of SGRBs are now a mature field. For the handful of mergers beamed toward us, we have rehearsed what needs to be done. On the other hand, off-axis and orphan SGRB afterglows, kilonovae, and radio transients are an uncharted territory. Both observational and theoretical progress is ongoing in leaps and bounds as we prepare for GW detectors to come online. Theoretical models continue to become more sophisticated with their predictions. Observationally, synoptic surveys in the optical are already uncovering entirely new classes of fainter and rarer transients. A suite of new radio facilities and radio transient searches are also coming online. For instance, wide-field low-frequency (say, <1 GHz) radio detectors (e.g., LOFAR, MWA, JVLA) should be sensitive to pre-merger coherent emission and coincident timing can be used to connect them to GW detections. Relatively higher sensitivity and higher frequency radio detectors (e.g., JVLA, ASKAP, Apertif) are well suited to searching for radio relic emission months to years after the GW detection.

5.3. *Detectability of EM Counterparts*

Next, we discuss the detectability of isotropic EM counterparts by optical and infrared telescopes. As quantified in Section 4.4, the localization and distance horizon distribution are dependent on the number of detectors and the threshold criterion in the GW network. We consider here the extreme cases for GW maximum detectable distances (Net3a and Net5b) and for sky error areas (Net3b and Net5a).

5.3.1. *Optical Facilities*

Astronomers have a diverse arsenal of optical telescopes worldwide. We limit the discussion here to only telescopes

Table 3
Optical Telescopes

Telescope	Aperture (m)	Field of View (deg^2)	Exposure (s)	Overhead (Readout)	Sensitivity (5σ mag in R band)	Reference
Zwicky transient facility	1.2	35	60	15	20.6	a
La Silla Quest	1.0	9.4 (80%)	60	30	20.5	b
Catalina real-time transient survey	0.7	8.0	30	18	19	c
Palomar transient factory	1.2	7.1	60	40	20.6	d
Pan-STARRS 1	1.8	7.0	60	3	22.0	e
Skymapper	1.35	5.62	110	20	21.5	f
CTIO-Dark energy camera	4.0	3.0	50	17	23.7	g
WIYN-One degree imager	3.5	1.0	60	30	23	h
CFHT-Megacam	3.6	0.9	60	40	23	i
Large Synoptic Survey Telescope	8.4 (6.7)	9.6	15	2	24.5	j
Subaru-HyperSuprimeCam	8.2	1.77	30	20	24.5	k

Notes.
[a] Kulkarni (2012).
[b] Hadjiyska et al. (2011).
[c] Drake et al. (2009).
[d] Law et al. (2009).
[e] See http://pan-starrs.ifa.hawaii.edu.
[f] See http://rsaa.anu.edu.au/observatories/siding-spring-observatory/telescopes/skymapper/skymapper-instrument.
[g] Bernstein et al. (2012).
[h] See http://www.wiyn.org/ODI/Observe/wiynodioverview.html.
[i] See http://www.cfht.hawaii.edu/Instruments/Imaging/Megacam/generalinformation.html.
[j] LSST Science Collaborations et al. (2009).
[k] See http://www.naoj.org/Projects/HSC/index.html and http://www.naoj.org/cgi-bin/img_etc.cgi.

with cameras larger than 1 deg^2 (given the large localization areas) and apertures larger than 1 m (given the faintness of a predicted counterpart). We consider current or scheduled-to-be operational telescopes. We divide telescopes into three categories: 1–3 m class telescopes, 4–7 m class telescopes, and 8–10 m class telescopes. Table 3 provides a summary of the sensitivity and FoV of each telescope and camera system.

Theoretical predictions of optical EM counterparts span orders of magnitudes in both predicted luminosity and predicted timescale (Section 5.1). To evaluate the relative merits of follow-up with different telescope facilities and to begin to define a search strategy, we need to make a conservative assumption on the nature of the counterpart. Hence, for the discussion below, we first assume that the optical counterpart of a NS–NS merger will be brighter than $M_{\mathrm{R}} = -14$ mag for at least 2 hr (later, we relax this assumption to -11 mag). Let us say a particular telescope takes three images at a separation of 1 hr, and each of these images has a 5σ depth of $M_{\mathrm{R}} = -14$ mag. Then, the counterpart will be discovered with high SNR (e.g., 12.5σ if the transient peaked at $M_{\mathrm{R}} = -15$ mag) in the first image, at least at 5σ in the second image, and possibly below a 5σ threshold in the third image. This is our "minimum" criterion for a secure detection. If the counterpart is either more luminous or evolves at a slower rate, it will only improve the security of our detection. We require a *minimum of two detections* to securely distinguish the optical counterpart from moving objects in our solar system (asteroids) and artifacts.

Telescope time is a zero sum game. A telescope with a given FoV of camera and a given aperture has to perform a three-way tradeoff between depth, cadence (how frequently the same field is observed), and area covered. Here, we assume that each telescope takes at least three sets of images separated by 1 hr. In this 1 hr, to attain the $M_{\mathrm{R}} = -14$ mag sensitivity for the most number of events, the telescope will either integrate longer on a given field to see events farther away or map a larger fraction of the localization area. If a telescope has a large aperture and small field camera, it will spend the 1 hr taking short exposures on a larger fraction of the localization area. If a telescope has a small aperture but a large field camera, it will spend the 1 hr stacking images to maximize integration time. It is precisely this choice that determines how many optical counterparts are detectable by a given telescope (*modulo* idealized observing conditions as we shall discuss).

We quantify the implications of this tradeoff on the number of detected NS–NS mergers in Figure 7(a) for a GW Net5b. For example, let us consider the role of CFHT in GW Net5b (green open squares in Figure 7(a)). In 100 s (60 s exposure + 40 s readout), CFHT can take a 0.9 deg^2 image with a depth of 23 apparent mag. In 1 hr, CFHT can take 36 exposures, hence there are 36 possibilities for the tradeoff. We discuss the first and last point on the curve of green squares. If CFHT spent the entire hour integrating on only one field, it would achieve a depth of 24.9 apparent mag and detect binaries with distances less than 615 Mpc (99%) but localization areas less than 0.9 deg^2 (2%). Instead, if CFHT spent the entire hour covering the large localization area and only spent 1 minute per field, it would achieve a poorer depth of 23 apparent mag and detect binaries only out to less than 250 Mpc (20%) but localization areas less than ∼32 deg^2 (73%).

Next, let us take the case of the 8 m class Subaru's HyperSuprimeCam (HSC, blue open squares). By spending only five exposures on a given field, the depth of HSC can cover 100% of distances of detected NS binary mergers. However, its smaller FoV camera limits the total area covered in one hour to 127 deg^2, i.e., 96% of mergers. LSST has the same depth but a larger camera, so it can detect 100% of mergers.

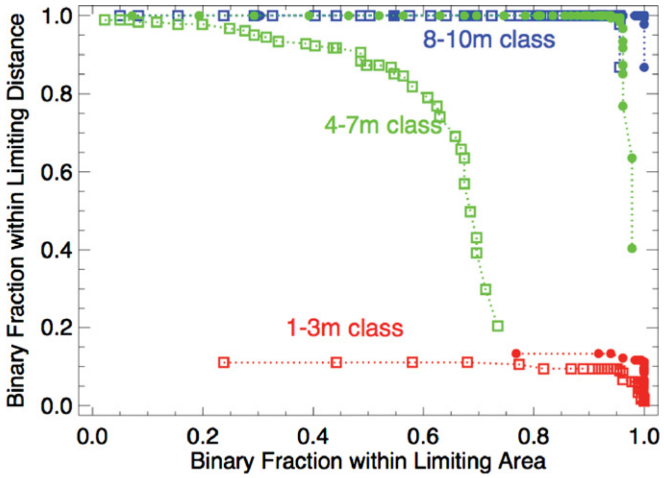

(a) NS-NS mergers, GW Net5b: M_R = -14

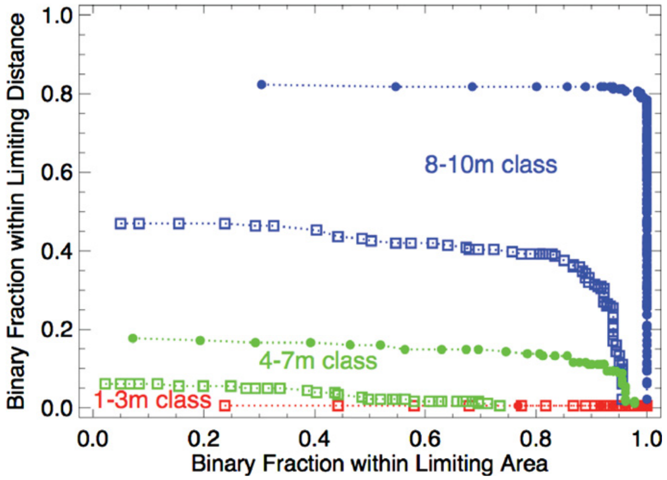

(b) NS-NS mergers, GW Net5b: M_R = -11

Figure 7. Top panel illustrates the depth vs. area tradeoff for optical telescopes when searching for NS–NS mergers detected by a GW Net5b, where the isotropic optical counterpart is assumed to be brighter than $M_R = -14$ for at least 2 hr. Bottom panel illustrates the depth vs. area tradeoff for optical telescopes when searching for NS–NS mergers detected by a GW Net5b and where the optical EM counterpart is assumed to be brighter than $M_R = -11$ for at least 2 hr. The different colors represent different telescope apertures: red is 1–3 m class, green is 4–7 m class, and blue is 8–10 m class telescopes. Open square is a small FoV camera and filled circle is a large FoV camera in that aperture class. Specifically: red square is PTF, red circle is ZTF, green square is CFHT, green circle is DECAM, blue square is HSC, and blue circle is LSST.

(A color version of this figure is available in the online journal.)

Let us next study the case of 1 m class ZTF (red filled circles in Figure 7(a)) in a GW Net5b. In less than five pointings, with its superior 35 deg^2 camera, ZTF can cover 100% of all localization areas. But its small aperture limits sensitivity to apparent 22.6 apparent mag or 210 Mpc, i.e., 10% of the mergers.

Now, we consider the implications of the isotropic optical counterpart being much less luminous, for instance $M_R = -11$ mag (Figure 7(b) and Table 4). The percentage of detectable counterparts goes down from 100% to 82% for LSST, from 96% to 42% for HSC, and 97% to 16% for DES.

Assuming the most optimal strategy is chosen for each merger in this simulation, we can compute the fraction of detectable optical counterparts by each telescope (Table 4). As exemplars, the smallest and largest FoV camera in each telescope aperture class is chosen. Initially, when there is a GW three-detector network, binaries would be detected closer in and the localizations would be poorer. The smaller telescopes with larger FoVs will play an important role (Figure 8(a)). In the era of a GW five-detector network, once localization is improved and maximal detectable distance pushed further back, the larger telescopes will be essential (Figure 8(b)).

Table 4

Relative Percentages of Isotropic, Optical Counterparts of GW-detected Mergers Detectable by Different Telescopes as a Function of GW Network, Triggering Criterion, and Peak Optical Luminosity

	PTF	ZTF	CFHT	DES	HSC	LSST
NS–NS merger & $M_R < -14$ mag						
GW Net3a	39	44	69	97	97	100
GW Net5a	34	41	95	98	98	100
GW Net3b	18	22	34	82	79	100
GW Net5b	10	13	61	97	96	100
NS–NS merger & $M_R < -11$ mag						
GW Net3a	0	0	19	39	86	100
GW Net5a	0	0	18	48	91	100
GW Net3b	0	0	8	16	45	93
GW Net5b	0	0	4	16	42	82
NS–BH merger & $M_R < -15.5$ mag						
GW Net3a	66	79	79	97	97	100
GW Net5a	63	72	93	100	93	100
GW Net3b	24	39	36	78	76	100
GW Net5b	22	28	56	96	94	100
NS–BH merger & $M_R < -12.5$ mag						
GW Net3a	3	3	17	79	93	100
GW Net5a	2	2	15	78	98	100
GW Net3b	1	1	5	33	47	98
GW Net5b	1	1	5	30	53	88

Note. Incorporation of realistic observing conditions (moon, Sun, weather, latitude, etc.) reduces efficiency by ~1/4.

Finally, we consider the case of NS–BH mergers. Given that NS–BH mergers will on average be detected a factor of two further away, but have predicted optical counterparts 1.5 mag brighter, we get similar detectability fractions as NS–NS mergers (Table 4).

We emphasize that the detectable fractions presented in Table 4 are relative and subject to two caveats. First, there would be tiling inefficiency and edge effects due to the irregular shapes of GW localization and the rectangular/circular fields of view of the EM cameras. Second, all optical telescopes in this discussion are subject to certain reality checks—they cannot observe too close to the Sun or too close to the moon, if it is cloudy or raining, or if the target is in the quadrant of sky not accessible from a given location. Typically, these factors amount to $(1/2) \times (2/3) \times (3/4) = (1/4)$ of the targets being visible at a given telescope on a given day, respectively.

We conclude that a network of telescopes at different longitudes, latitudes, and mountain tops would maximize the odds of follow-up. Hence, the numbers presented here should only be interpreted as illustrative of the relative detectability by different telescopes.

5.3.2. Infrared Facilities

Recent theoretical calculations of kilonovae opacities suggests that a significant fraction of the luminosity may be emitted in the redder bands beyond 1 μm (Barnes & Kasen 2013). Unfortunately, our current suite of near-infrared facilities is not as wide field as the optical with no camera larger than a square degree.

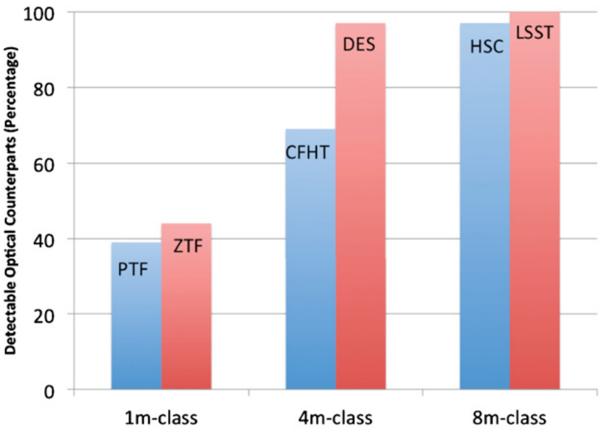

(a) GW Net3a

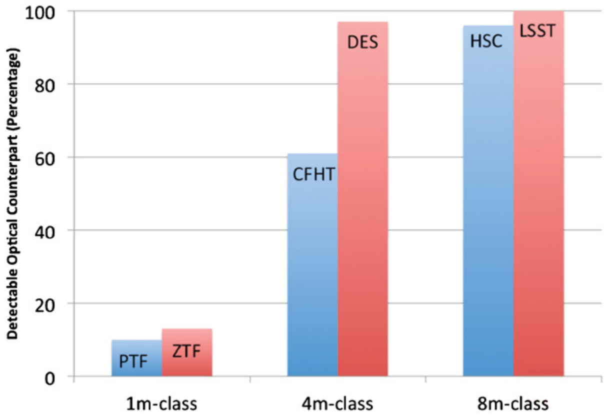

(b) GW Net5b

Figure 8. Relative fraction of detectable isotropic optical counterparts to NS–NS mergers for GW Net3a and Net5b. Note that even the small aperture wide field telescopes are sensitive to a significant fraction, and DES and HSC are almost as sensitive as LSST.

(A color version of this figure is available in the online journal.)

Currently, the two widest field infrared facilities are the 0.594 deg^2 VIRCAM on the 4.1 m VISTA telescope and the 0.19 deg^2 WFCAM on the 3.8 m UKIRT telescope. Fortunately, efforts are underway to build a 6.5 m SASIR telescope with a 0.2–1 deg^2 camera (SASIR 2012). Moreover, unlike VIRCAM and WFCAM, SASIR is expected to have a contiguous focal plane and simultaneously image in *YJHK* bands.

Efforts are also underway to build two wide-field infrared satellites—WFIRST (Green et al. 2012) and Euclid (Amendola et al. 2012). A set of three WFIRST fields is expected to cover 2 deg^2 and 18 minutes per field will give a 5σ depth of $H \sim 25.9$ mag for imaging and $H \sim 23.5$ mag for low-resolution prism spectroscopy. Euclid would need four fields to cover 2 deg^2 and achieve depths of $H \sim 25.6$ mag and $H \sim 21.4$ mag in the grism mode in the same time. Both missions are constrained to observe $\sim 90^\circ$ away from the Sun (Hirata et al. 2012).

We remind the reader that the median–maximum localization of Net 3b is 55–180 deg^2 and Net 5a is 7–120 deg^2 (Table 2). Hence, the infrared follow-up will require an extremely large number of pointings to tile the area and will be limited to the best localized binaries.

6. IDENTIFYING EM COUNTERPARTS

Detection of candidate EM counterparts is only the first step. The most pressing question for EM telescopes looking at vast sky areas will be whether the transient objects are true GW emitters or false-positive signals mimicking an EM counterpart. For instance, the optical sky is so dynamic that there will be hundreds of foreground and background false positives associated with any detection. Foreground signals are, for example, M-dwarf flares, CVs, and other stellar variables in the Milky Way. The foreground rates, therefore, depend strongly on the Galactic latitude and have a wide range of amplitudes and timescales. Background signals are supernovae (SNe) and active galactic nuclei (AGNs) at higher redshift than the GW detectable distance horizon for NS binary mergers of ∼200 Mpc–1 Gpc. Thanks to systematic optical synoptic surveys, rate estimates of different classes of SNe occurring in a range of galaxy hosts now exist; for instance, core-collapse SNe rate is $7.1\ (\pm 0.1) \times 10^{-5}\ \mathrm{Mpc}^{-3}\ \mathrm{yr}^{-1}$ (see, e.g., Leaman et al. 2011; Li et al. 2011a, 2011b).

Hence, panchromatic follow-up (especially optical spectroscopy) is critical to unambiguously associate the counterpart with the GW signal. Given predicted optical light curve evolutions, the timescale for spectroscopic follow-up should be within hours to a day. There are a large number of telescopes in the 3–5 m class range that can easily take low-resolution spectra of transients brighter than 21 apparent mag. However, optical counterparts will likely be in the regime where the transient is fainter than 22 apparent mag and a >6 m class telescope will be needed for spectroscopy. The list of such telescopes is rather small: the twin Magellan 6.5 telescopes, the MMT 6.5 m telescope, the twin Gemini 8 m telescopes, the four VLT 8 m telescopes, the HET 9.2 m telescope, the SALT 9.2 m telescope, and the twin Keck 10 m telescopes. Efforts are underway to build even larger 20–30 m class telescopes: GMT, TMT, and ELT. Spatial coincidence with a nearby Galaxy will distill the large number of counterpart candidates to a small number that can be promptly followed up spectroscopically (Kulkarni & Kasliwal 2009).

To illustrate the diversity of follow-up scenarios, we consider below five case studies of NS–NS mergers. In each case, we discuss optimal strategies for identifying the EM counterpart of the NS binary merger. Finally, we discuss how we can leverage volume information to aid EM follow-up strategies for a *population* of NS binary mergers.

6.1. Individual Binaries

We first examine sky localization and volume errors for one beamed NS–NS binary merger at 391 Mpc, and four NS–NS mergers that have distances less than 200 Mpc and lie within the CLU catalog used in this work. We choose the five NS–NS mergers described below because their geometric properties or sky locations represent useful bounds that illustrate the challenges for any EM follow-up. The five case studies comprise NS–NS mergers with (1) an orbital angular momentum vector face-on toward the Earth, (2) a close-by event, (3) a source position at low Galactic latitude, (4) a source position at high Galactic latitude, and (5) a source position in a dense galaxy cluster environment.

6.1.1. Case Study I: Beamed Binary Merger at 391 Mpc

We consider the case of a binary merger beamed toward us. Given the Malmquist bias (Section 4.3), these binaries are at threshold and are thus, on average, located farther away. Out of 200 randomly sampled mergers detected with a GW Net3a, the distances of beamed NS–NS mergers are 391 Mpc, 506 Mpc, 560 Mpc, and 564 Mpc. Illustrated by Figure 9, using GW networks 3 and 5, the localization for the closest of these binaries

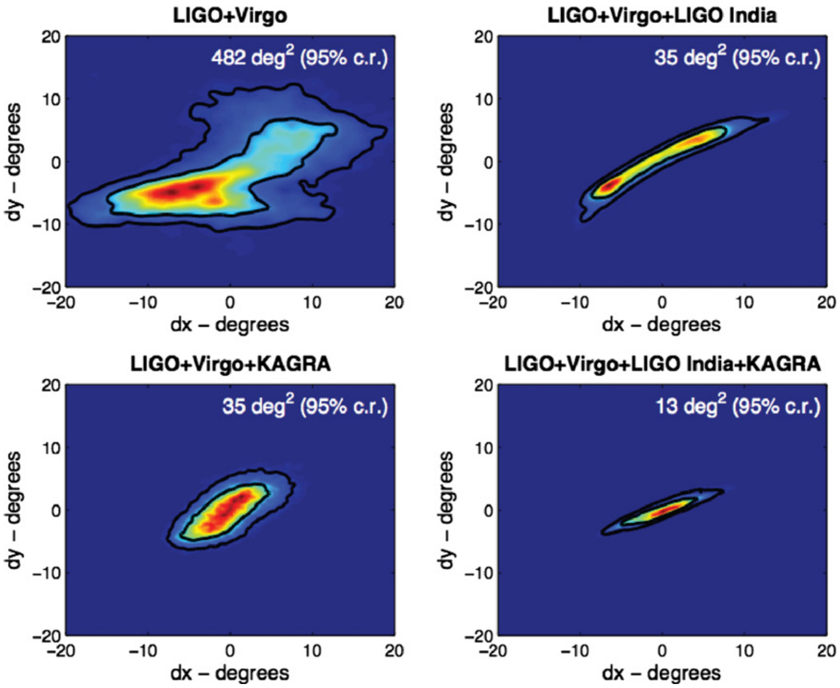

Figure 9. Sky localization errors at 95% c.r. using different GW networks for a NS–NS binary merger located at ∼390 Mpc whose orbital angular momentum is directly face-on to the Earth.

(A color version of this figure is available in the online journal.)

is 483 deg^2 (95% c.r.) and 13 deg^2 (95% c.r.), respectively. Current γ- and X-ray satellites are easily sensitive to SGRBs at these distances (the furthest detected *Swift* SGRB is 090426 at a redshift of 2.68 or 22 Gpc). Advantageously, these satellites have large instantaneous FoVs. Moreover, given the precise timing of the gamma-ray burst, false-positive signals are not a concern (Kanner et al. 2012). If a precise position (e.g., with XRT onboard the *Swift* satellite or with MIRAX-HXI) is available, prompt follow-up to look for the radio and optical afterglows (which will be much brighter than a kilonova signal but decay as a power law in time) will be tractable.

Unequivocally, wide-field γ- and X-ray satellites (e.g., *Fermi*, *Swift*, Lobster, *MAXI*, MIRAX-HXI) are currently the most promising wavelengths to search for EM counterparts of beamed NS–NS and NS–BH mergers. However, as Table 1 shows, the *beamed* NS–NS mergers are a very small fraction (∼1.5%–∼3%) of the total GW-detected population. Hence, coincident GW and EM observations of beamed NS binary mergers will be rare.

6.1.2. Case Study II: Close-in Binary at 70 Mpc

Nearby (<100 Mpc) NS binary mergers provide excellent laboratories in which to study strong-field gravity astrophysical processes using joint GW and EM observations. Such a “golden binary” should result in high SNR detections in GWs and multiwavelength EM waves, enabling excellent characterization of the physical properties of the progenitor and post-merger remnants.

Let us consider a simulated NS–NS merger located at 69 Mpc. A GW network 3 measures the source position to 0.6 deg^2. A GW network 5 reduces this sky area error by a factor of a couple to 0.3 deg^2 (Figure 10). Using GW network 1, the distance range is from 43 to 73 Mpc at 95% c.r. With relatively small localization errors and distance measures, the number of astrophysical false-positive events that require classification will be nearly zero. In addition, assuming that the NS binary merger occurred near or within a galaxy, cross-correlating GW localization errors with galaxy catalogs, such as the Census of the Local Universe (CLU), leaves us with only a handful of candidates for galaxy hosts. As Figures 11(a) and (b) show, we expect to see five galaxies within an error cube of 2 deg × 2.5 deg × 55 Mpc. The CLU is currently 65% complete within this distance bin and efforts are underway to make this catalog more complete. With GW network 5, Figure 11(b) shows that we should be able to identify uniquely one host galaxy using full 3D-marginalized volumes computed at 95% c.r. (this is also the case using the low-latency GW volumes described in Section 4.5).

Therefore, for such a well-localized nearby “golden” binary (with distances <100 Mpc), we can undertake pointed host galaxy follow-up and are no longer limited to large FoV cameras. Moreover, we can observe deeper and use a faster cadence than for an average faint binary. Intensive panchromatic follow-up with a wide array of facilities in the optical, infrared, radio, and X-ray would ensure that we leave no stone unturned in studying the EM counterpart to a golden binary. We note that only 10% of NS–NS mergers seen by GW Net3a are golden and will have true distances less than 100 Mpc. Using GW Net5b, we note that only 1.5% of binaries will be golden, but they will have high SNR detections in GWs and EM waves.

6.1.3. Case Study III: Low Galactic Latitude and at 125 Mpc

Let us consider the case of a binary with an inclination angle of 150°, a distance of 125 Mpc, and located very low on the Galactic plane (latitude of $-0\overset{\circ}{.}11$, longitude of $63\overset{\circ}{.}4$). Using GW network 3, the sky localization of the merger is 1.8 deg^2 at 95% c.r. GW network 5 reduces the sky area error to 1.3 deg^2.

Without any distance information, we would need to search for the isotropic $M_R = -14$ optical counterpart signal out to 450 Mpc, i.e., 24.3 apparent mag. The number of background

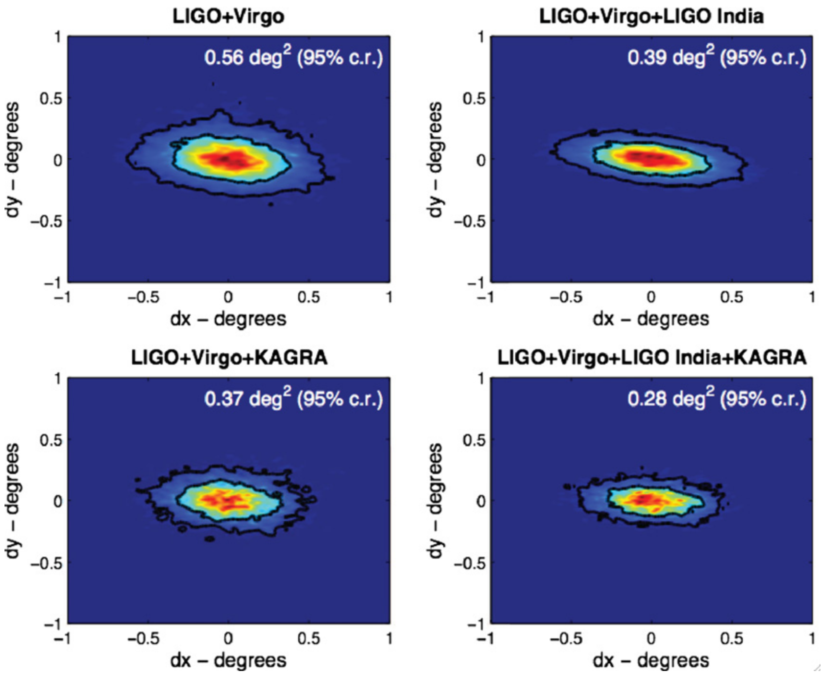

Figure 10. Sky localization errors at 95% c.r. for a NS–NS merger located at 69 Mpc with an inclination angle = 150° observed by different GW networks. The expected SNRs at LIGO Hanford, LIGO Livingston, Virgo, LIGO India, and KAGRA are 35, 47, 26, 24, and 36, respectively.

(A color version of this figure is available in the online journal.)

supernovae active in this area at this time would be ∼120 and the number of foreground M-dwarf flares active would be ∼76. Unfortunately, at such a low Galactic latitude, galaxy catalogs are most incomplete and cannot be effectively used to reduce false positives.

However, the derived GW low-latency localization volume can help reduce false positives. Using GW network 3, the distance measure in this volume ranges from 72 Mpc to 142 Mpc at 95% c.r. (Figure 12). The reduction in volume from the maximum detectable distance of 450 Mpc to 142 Mpc is 97%! Instead of searching down to 24.3 mag, we only need to search to 21.8 mag. This reduces the background and foreground false positives to <10.

Another effective strategy to deal with foreground false positives is to use a quiescent star catalog (in the optical or infrared) that is about 2 mag deeper than the search depth (Stubbs 2008). Several synoptic surveys (e.g., SDSS, PTF, Pan-STARRS, and Skymapper in the optical; VISTA, UKIDSS, and *WISE* in the infrared) are underway to give us such a catalog. Moreover, some of these surveys will also provide a multi-year historic baseline for variable sources.

In practice, the limiting factor for follow-up of such a merger would be the crowding and large line-of-sight extinction: ∼8 apparent mag in *R* band and 1 apparent mag in *K* band. Near-infrared follow-up would be much easier than optical follow-up. The percentage of GW detected mergers with a Galactic latitude less than 5° is ∼9% and Galactic latitude less than 10° is ∼18%.

6.1.4. Case Study IV: High Galactic Latitude and at 139 Mpc

The previous three case studies represent a subset of binaries. Let us now consider a canonical binary, which is not beamed, not very close by, and not too low on the Galactic plane. This binary has an inclination angle of 64°, a distance of 139 Mpc, and a Galactic latitude of −66°. We expect no EM counterparts at γ- and X-ray wavelengths. Using GW network 3, GW measurements can localize the event to 19.5 deg^2 on the sky (using GW network 5, the localization error improves to 8 deg^2).

Without any GW distance constraints, we would need to search for an optical counterpart brighter than $M_{\rm R} = -14$ to a horizon distance of 450 Mpc, i.e., 24.3 apparent mag. Therefore, in a 19.5 deg^2 error circle, the extragalactic false-positive number will be ∼1300. The Galactic false-positive number will be ∼100.

One strategy is to identify the EM counterpart from a false positive based on the light curve signature. An outburst due to a NS binary merger would be a one-time occurrence. If we have a good historic light curve of the candidates, foreground false positives and AGNs would show previous eruptions. Unfortunately, at a depth of 24 apparent mag, this may not be the case for most of the sky until LSST has been operating for a few years. We can also use the theoretical prediction that optical counterparts, such as kilonovae, evolve faster than supernovae in the same field. Unfortunately, if we wait too long to obtain multiple epochs, the EM counterpart may fade to a level where it is too faint for spectroscopic follow-up. We could also use theoretical predictions that kilonovae may be redder than supernovae in the same field. Unfortunately, given the depth needed and large localization areas, there may not be enough time to obtain data in multiple filters.

To reduce the number of false positives, a simple approach is to assume that the merger is spatially coincident with or nearby a galaxy within the distance reach of the GW network. Galaxies occupy a very small area on the sky. There are only 228 known galaxies in the error circle within 450 Mpc. Allowing a large radius including 50 kpc around each galaxy, the total area is 60 arcmin^2 and the reduction in false positives is a factor of 1200! Allowing an even larger radius including 100 kpc around each galaxy, the total area is 240 arcmin^2 and the reduction in false positives is still a factor of 300. Unfortunately, the current galaxy catalog is grossly incomplete and it is imperative that efforts be made to complete it.

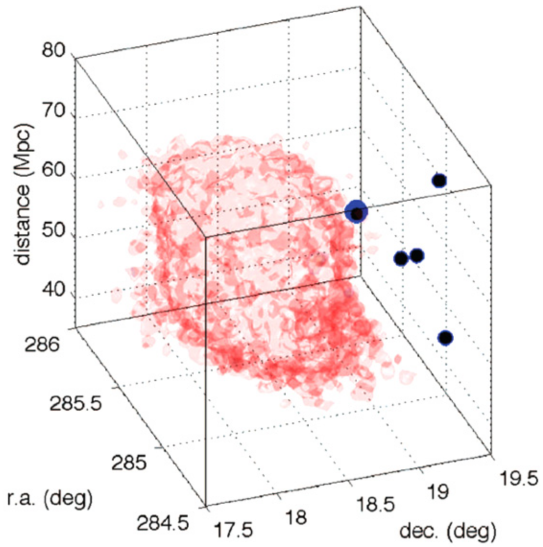

(a) GW network 3

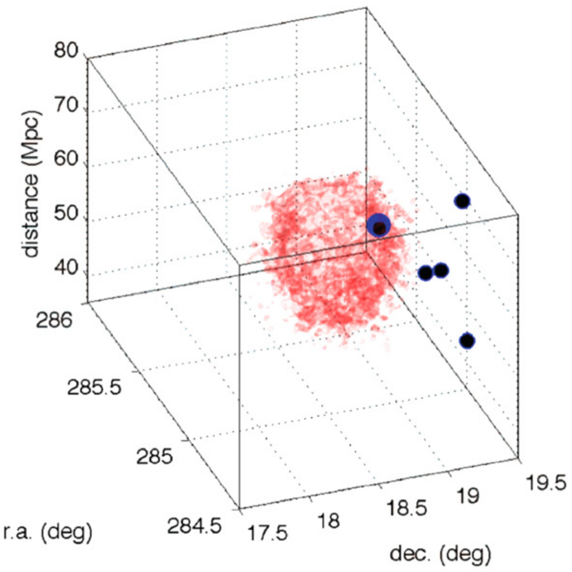

(b) GW network 5

Figure 11. Volume errors at 95% c.r. for a NS–NS merger located at 69 Mpc with inclination angle = 150° observed by GW networks 3 and 5. The blue circle marks the merger's true position and the black circles denote the five galaxies within the cube's volume. Note that the above circles are not to scale.

(A color version of this figure is available in the online journal.)

Furthermore, we can leverage our localization volume constraint to further reduce the number of relevant host galaxies. Using GW network 3, the merger's distance is measured to be between 108 Mpc and 228 Mpc, the volume is smaller than between 0 Mpc and 450 Mpc by 88% (Figure 13(a)). A smaller volume would correspond to a smaller number of galaxies. In this case, 73 galaxies are known to lie in the localization volume. Using GW network 5, the merger's distance is measured to be between 117 Mpc and 230 Mpc and currently, ∼37 galaxies are known in this volume (Figure 13(b)). This list of galaxies is incomplete by a factor of two. If we had a complete catalog of galaxies, and for cases where the number of galaxies was less than a few tens, we would even consider targeting galaxies individually. We would not require a large FoV camera, paving the way for using infrared, radio, and X-ray facilities.

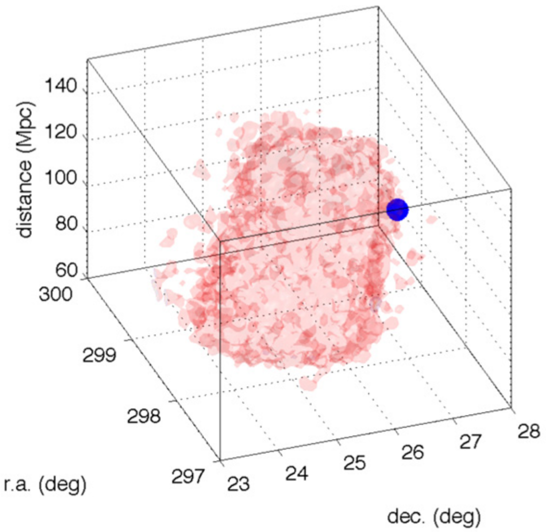

(a) GW network 3

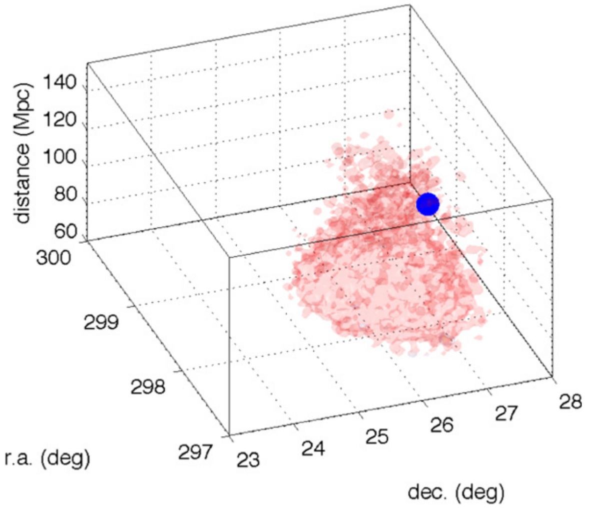

(b) GW network 5

Figure 12. Volume errors at 95% c.r. for a NS–NS merger located at 125 Mpc with inclination angle = 150° observed by GW networks 3 and 5. The blue circle (not to scale) marks the binary's true position. Due to the low Galactic latitude, there are no known galaxies within the volume shown. Using network 3, the GW distance measure ranges from 72 Mpc to 142 Mpc (95% c.r.); the reduction in volume is 97%.

(A color version of this figure is available in the online journal.)

6.1.5. Case Study V: Dense Galaxy Cluster Environment at High Galactic Latitude at 115 Mpc

For our final case study, we choose a simulated NS–NS binary merger event that occurs in an extremely dense galaxy cluster (ABELL 4038). Here, the use of localization volumes to target individual galaxies is not feasible as the number of galaxies is too large. However, using a galaxy catalog to prioritize follow-up can still reduce false positives by orders of magnitude.

This specific binary has a distance of 115 Mpc and Galactic latitude and longitude of −75°.8 and 25°.7, respectively. With GW network 3, its sky localization can be measured to 18.8 deg^2 and its distance measure ranges from 110 Mpc to 269 Mpc (Figure 14(a)). The upper measure of the distance (at 95% c.r.) is greater than the maximum distance of 200 Mpc used in CLU. Assuming only a horizon distance of 200 Mpc and using the CLU catalog, we find 780 galaxies comprising an

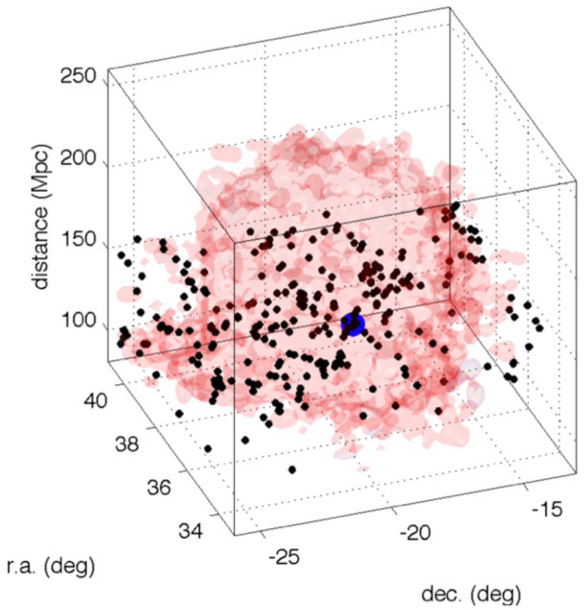

(a) GW network 3

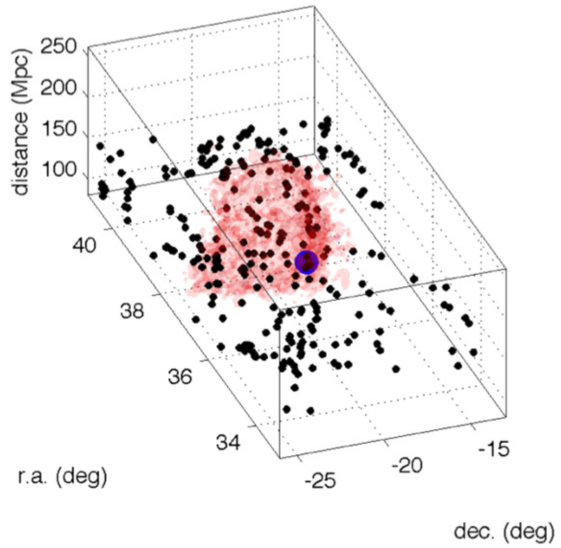

(b) GW network 5

Figure 13. Volume errors at 95% confidence interval for a NS binary merger located at 139 Mpc with inclination angle = 64° observed by GW networks 3 and 5. The blue circle marks the binary's true position and the black circles denote the 279 galaxies within the cube's volume. Note that the circles above are not to scale.

(A color version of this figure is available in the online journal.)

area of 1070 arcmin^2 within such an area of the sky. If we then include our lower measure of the distance (at 95% c.r.), we find 410 galaxies comprising an area of 560 arcmin^2. Increasing the network from three to five interferometers, its sky localization improves to 14.4 deg^2 and its distance measure ranges from 97 Mpc to 155 Mpc (Figure 14(b)). Using CLU, we then find 390 galaxies comprising an area of 530 arcmin^2 within such an area of the sky.

In such a dense galactic environment, targeting hundreds of galaxies individually is not feasible. However, the reduction of false positives is still significant. Specifically, a snapshot of 18.8 deg^2 out to 450 Mpc would give 1250 background supernovae. Restricting the search to candidates spatially coincident

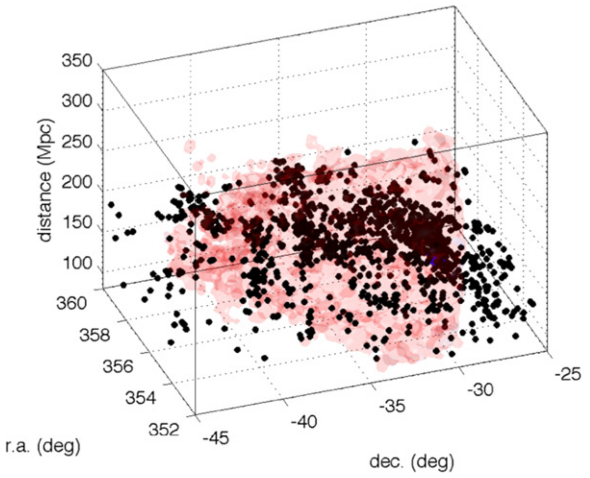

(a) GW network 3

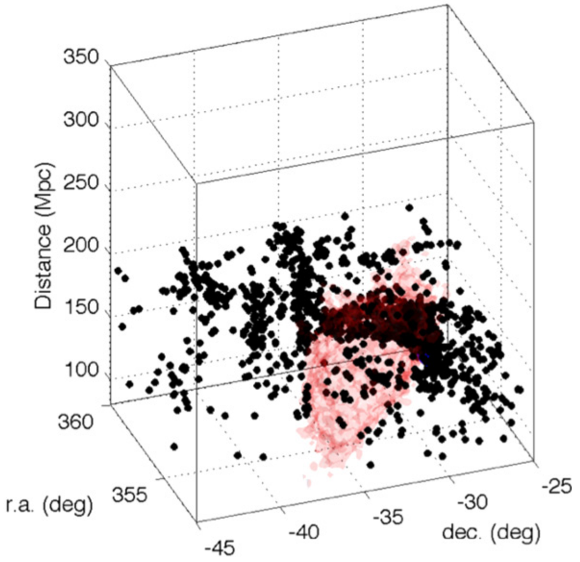

(b) GW network 5

Figure 14. Volume errors at 95% confidence interval for a NS–NS binary merger located at 115 Mpc with inclination angle = 87° observed by GW networks 3 and 5. The blue circle marks the binary's true position and the black circles denote the 1350 galaxies within the cube's volume. Note that the circles above are not to scale.

(A color version of this figure is available in the online journal.)

with nearby galaxies (i.e., 1070 arcmin^2) reduces the false positives to 20. Further imposing the volume constraint of 269 Mpc reduces the false positives to four events.

6.2. Astrophysical Populations

As discussed in Section 6.1, the combination of GW distance information, GW sky localization, and galaxy catalogs could help reduce the number of galaxies that are possible hosts of the NS binary merger event and the number of false positives. The use of spatial coincidence with galaxies in turn could have a substantial effect in reducing the number of false-positive transients that need to be considered as possible NS–binary merger events (Kulkarni & Kasliwal 2009). Alternatively, if we can limit the number of host galaxy candidates to a few as in the case of a golden nearby GW merger, targeted follow-up opportunities for individual galaxies becomes a possibility.

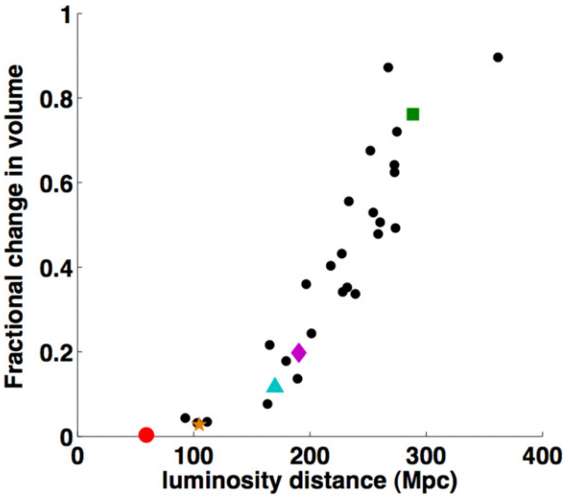

(a) NS-NS binary mergers observed by GW Net3a

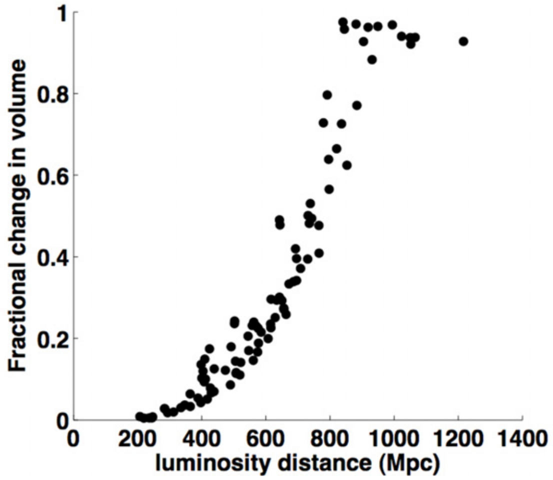

(b) NS-BH binary mergers observed by GW Net5b

Figure 15. Fractional reductions in volume for a detected sample of NS–NS mergers observed by GW Net3a (top panel) and NS–BH mergers observed by GW Net5b (bottom panel). This fraction is the ratio of the volume encompassed by GW distance measures (Figure 6 in Section 4.5) and the volume encompassed within the GW maximum detectable distance. Each circle represents a detected NS binary merger. The different colors represent different case studies of NS–NS mergers examined in Section 6.1: the green square is Case I (beamed binary), the red circle is Case II (a nearby binary), the light blue triangle is Case III (a merger at low Galactic latitude), the purple diamond is Case IV (a merger at high Galactic latitude), and the orange star is Case V (a binary in a dense galaxy cluster environment).

(A color version of this figure is available in the online journal.)

Following from Figures 6(a) and (b), next, we compare how well we fare when computing GW volumes either using the event's distance measure or using only the GW horizon distance. In particular, we compute $r_{\rm vol}$ the fractional change in volume:

$$r_{\rm vol} = \frac{(\min[d_u, d_h])^3 - d_l^3}{d_h^3}, \qquad (8)$$

for samples of NS binary mergers detected using different GW networks and triggering criteria (see Figures 15(a) and (b)).

We find that the fractional change correlates with distance to the binary and the reduction is higher for nearer binaries. Specifically, for NS–NS mergers, the fractional change in volume is $<$60% for those events located within 200 Mpc ($\sim$1/3 of the detected binaries). For NS–BH binaries, the fractional change in volume is $<$60% for those events located within 700 Mpc ($\sim$1/2 of the detected binaries).

The implications for search strategies are as follows. In cases where the upper limit of localization volume is much less than GW maximum detectable distance (cf. case studies 2, 3, and 4), the EM counterpart search can be to brighter apparent magnitudes. This significantly reduces false-positive numbers and spectroscopic follow-up is easier. More frequent are the cases where knowledge of the lower distance limit reduces the total number of host galaxies.

The number density of galaxies is 0.6 deg^{-2} Mpc^{-1} at $z = 0.1$ and $L > 0.1\,L_\star$ and scales with z^2 (Blanton et al. 2003). For a median localization of 10 deg^2 and out to a distance of 200 Mpc, the number of galaxies is $\sim$80. The median size of a galaxy is [0.8, 0.4, 0.2] arcmin^2 at [50, 100, 200] Mpc, respectively. The diameter assumed here is for the surface brightness contour of 25 mag arcsec^{-2}. This corresponds to a projected offset (offset$_{\rm kpc}$ = size$_{\rm rad}$ × distance$_{\rm kpc}$) of [7.3, 10.8, 14.0] kpc at [50, 100, 200] Mpc, respectively. Thus, the total area occupied by 80 galaxies is 0.004 deg^2, a factor of 2500 smaller than the localization. We can easily search 10 times the size of the galaxy to accommodate large kicks of the order of a hundred kiloparsecs (e.g., Fong et al. 2010; Kasliwal et al. 2012) in NS–NS mergers and still gain a factor of 25 in terms of reduction of false positives. However, if the kicks are over a megaparsec (Kelley et al. 2010), we cannot use the positions of host galaxies to reduce false positives.

Efforts are underway to complete the CLU galaxy catalog using four narrowband filters on the Palomar 48 inch Schmidt telescope. This will boost the completeness from 50% to 85% of the *B*-band light at 200 Mpc in the three-quarters of the sky accessible from Mount Palomar. Note that this distance limit is well matched for majority of NS–NS binaries detected by GW Net 3a. However, particularly for NS–BH binaries, we should consider an even larger effort to complete galaxy catalogs out to several hundred megaparsecs.

7. CONCLUSIONS AND DISCUSSION

Observing compact-object binary mergers in both GW and EM will be challenging. GW interferometers will only be able to localize the merger to sky errors ranging from tens to hundreds deg^2. In addition, the estimated rates of GW-detected compact binary mergers span several orders of magnitude from zero to hundreds of mergers per year. Theoretical predictions of EM signatures from the optical to radio is also an active area of research and model estimates vary significantly. Finally, our characterization and understanding of the transient sky at different wavelengths, timescales, and sensitivity remains incomplete.

In this paper, we present the first comprehensive end-to-end simulation of the detectability and identification of NS binary mergers with GW and EM facilities. Our simulation comprises: the construction of astrophysically distributed populations of GW-detectable NS–NS and NS–5-$M_\odot$-BH binary mergers, GW source characterization using different GW detector networks and triggering criteria, establishing the detectability of plausible EM counterparts by upcoming or current telescopes (particularly, optical), and identifying the GW event among the few to many astrophysical false-positive transients in different wavelengths. The extent of our analysis is naturally dependent on the assumptions made: an underlying population of non-spinning NS–NS or NS–5-$M_\odot$-BH binary mergers, GW instrumental Gaussian noise with each interferometer operating continuously, negligible GW systematic errors arising from the GW waveform and instrument calibration, a high availability factor for telescopes to follow-up GW mergers, and idealized optical observing conditions.

Our work is novel in six principal ways. First, we construct GW-detected populations of astrophysically distributed NS binary mergers using CLU (a volume-limited local universe galaxy catalog out to 200 Mpc), instead of at fixed SNR or distances as in earlier works. Second, we incorporate advanced LIGO detectors using optical squeezed light into our analysis. Third, we compute explicit marginalized 3D GW volumes using MCMC. Fourth, we consider how GW volumes can assist follow-up by optical telescopes and other EM facilities. Fifth, we quantify the tradeoff between depth and area for a variety of optical telescopes, including 4–7 m class and HSC telescopes for the first time. Sixth, by examining individual NS binary mergers, we suggest how to pinpoint the GW event among a possible plethora of astrophysical Galactic and extragalactic false positives.

By expanding the parameter space of NS binary populations and GW networks, we show that GW detectable distances and sky area errors may range an order, or several orders of magnitudes, respectively. From our case studies of GW-detected NS binary mergers, we find that:

1. Thanks to the GW Malmquist effect, the fraction of NS binary mergers beamed toward us (with $\theta_{\rm j} < 6^\circ$) is boosted to large distances (400 Mpc–1.3 Gpc). However, we have shown empirically that the fraction is still tiny (1%–2.5%). For this subset of events, the easiest identifiable EM counterpart would be a contemporaneous SGRB. All-sky γ-ray detectors are essential to ensure joint GW and EM observations. Optical squeezing implemented in GW interferometers will also increase the beamed fraction by a further factor of 9–10.
2. For the small number of golden nearby binaries (<100 Mpc), which have small GW localizations given the high SNRs of GWs, we should intensively follow up such events at all wavelengths. While the number of detected golden binaries is independent of network, the total GW-detected fraction ranges from 2% to 10% from GW Net3a to GW Net5b. The number of false positives in their small localization areas or volumes should be small (Section 6.1.2).
3. For the majority of binaries which are neither beamed nor nearby, the challenges in detecting the isotropic optical counterpart are surmountable by optimizing the depth versus area tradeoff. Initially, we expect small telescopes (especially given their larger number and wide-field cameras) to play an important role in detecting counterparts. GW networks with fewer detectors will have poorer localizations and lower distance sensitivity. Small telescopes have strength in numbers and can be expected to be more flexible for rapid follow-up for GW triggers. Later, with increasing detector numbers and instrument sensitivity and use of coherent triggers, GW networks will have higher distance sensitivity and improved localizations, larger telescopes will be essential (Section 5.2.1). Given weather and limited sky accessibility of optical telescopes (due to Sun constraints and altitude constraints), we advocate for a worldwide network of telescopes of different sizes with wide-field cameras spread across different latitudes and longitudes. Furthermore, we advocate the building of larger FoV infrared cameras.

Our simulation and detailed case study analysis motivate us to search for EM counterparts to GW binaries. We find that although there are challenges, they are surmountable by timely advance preparation. Hence, we conclude here with four action items that will better prepare us to securely identify the detected EM counterpart.

1. We should complete host galaxy catalogs out to $z \sim 0.1$ as much as possible to increase the possibility of identifying an EM counterpart through two different means. Spatial coincidence with a nearby galaxy can quickly eliminate false positives for a subset of NS binary mergers by orders of magnitude. This is critical to prioritize candidates for prompt spectroscopic and panchromatic follow-up (Sections 6.1.4, 6.1.5, and 6.2). Together with low-latency GW volume errors, in some cases, the number of galaxies can be reduced to a tractable number for possible targeted follow-up with relatively smaller field-of-view facilities, e.g., radio, infrared, X-ray, large aperture optical telescopes (Sections 6.1.2, 6.1.4, and 6.2). An ongoing effort is the Census of the Local Universe (CLU) using narrowband filters (Hα) on the Palomar 48 inch. Another planned survey (H I) is WALLABY with ASKAP in the Southern Hemisphere (D. Kaplan 2012, private communication).
2. We should construct deep (∼26 apparent mag) all-sky quiescent stellar source catalogs which would help eliminate foreground false positives, particularly at low Galactic latitudes (Section 6.1.3). We estimate that we will require catalogs that are approximately 2 mag deeper than the EM counterpart and span optical and infrared wavelengths. Current ongoing efforts may not be deep enough, e.g., SDSS, PTF, Pan-STARRS, SkyMapper, *WISE*, VISTA.
3. We should rehearse the search for transients in large sky localizations. For example, the successful identification and follow-up of an optical afterglow of a *Fermi*/GBM GRB in a 3 deg^2 error circle (cf. GRB120716A; Cenko et al. 2012) is encouraging. Such efforts are a full dress rehearsal for elusive EM counterparts in GW constrained large swaths of the sky (S. Kulkarni 2012, private communication).
4. We should continue to construct a complete inventory of transients within several hundred megaparsecs. In just the past few years, we have uncovered multiple, new classes of optical transients, which are fainter, faster, and rarer than supernovae (e.g., Kasliwal 2011). We may indeed even be lucky enough to see an EM counterpart to a NS binary merger prior to hearing the GWs!

In summary, given the diversity of properties and locations of possible EM counterparts and challenges in their identification, we advocate a *comprehensive, multiwavelength, multi-pronged* approach to observing compact binary mergers in GWs and EM waves.

M.M.K. acknowledges generous support from the Hubble Fellowship and Carnegie-Princeton Fellowship. A.G. thanks the Summer Undergraduate Research Fellowship program at Caltech.

We are very grateful to Jean-Michel Désert, Dale Frail, Chris Hirata, Shri Kulkarni, and Setu Mohta for careful reading of the manuscript. We thank Ernazar Abdikamalov, Paul Groot, Gregg Hallinan, Brian Metzger, Sterl Phinney, Tony Piro, Tom Prince, Jon Sievers, and Linqing Wen for useful discussions. S.M.N. thanks the ITC for hospitality and discussions there with Edo Berger and Josh Grindlay. We thank Anand Sengupta and Tarun

Souradeep for providing LIGO India's (previously referred to as IndIGO) position and orientation. We thank Haixing Miao for providing the anticipated advanced LIGO noise curve with optical squeezing and Masaki Ando, Larry Price, and Stan Whitcomb for KAGRA and LIGO follow-up references. We thank Neil Gehrels, David Kaplan, Peter Nugent, and Fang Yuan for providing specifications of Lobster-ISS, WIYN, La Silla Quest, and Skymapper, respectively. Some of the simulations were performed using the Sunnyvale cluster at CITA. Part of this work was performed at the Jet Propulsion Laboratory, California Institute of Technology, under contract with the National Aeronautics and Space Administration. Government sponsorship acknowledged.

REFERENCES

Abadie, J., Abbott, B. P., Abbott, R., et al. 2010, CQGra, 27, 173001
Abadie, J., Abbott, B. P., Abbott, R., et al. 2012a, PhRvD, 85, 082002
Abadie, J., Abbott, B. P., Abbott, R., et al. 2012b, A&A, 541, A155
Accadia, T., Acernese, F., Antonucci, F., et al. 2011, CQGra, 28, 114002
Ajith, P., & Bose, S. 2009, PhRvD, 79, 084032
Amendola, L., Appleby, S., Bacon, D., et al. 2012, arXiv:1206.1225
Barish, B. C., & Weiss, R. 1999, PhT, 52, 44
Barnes, J., & Kasen, D. 2013, AAS, 221, 346.04
Berger, E. 2010, ApJ, 722, 1946
Berger, E. 2011, NewAR, 55, 1
Berger, E., Price, P. A., Cenko, S. B., et al. 2005, Natur, 438, 988
Bernstein, J. P., Kessler, R., Kuhlmann, S., et al. 2012, ApJ, 753, 152
Blanchet, L. 2006, LRR, 9, 4
Blanton, M. R., Hogg, D. W., Bahcall, N. A., et al. 2003, ApJ, 592, 819
Bloom, J. S., Holz, D. E., Hughes, S. A., et al. 2009, arXiv:0902.1527
Bloom, J. S., Prochaska, J. X., Pooley, D., et al. 2006, ApJ, 638, 354
Burrows, D. N., Grupe, D., Capalbi, M., et al. 2006, ApJ, 653, 468
Cannon, K., Cariou, R., Chapman, A., et al. 2012, ApJ, 748, 136
Cenko, S. B., Ofek, E. O., & Nugent, P. E. 2012, GCN, 13489, 1
Chandra, P., & Frail, D. A. 2012, ApJ, 746, 156
Chawla, S., Anderson, M., Besselman, M., et al. 2010, PhRvL, 105, 111101
Chen, H.-Y., & Holz, D. E. 2012, arXiv:1206.0703
Coward, D., Howell, E., Piran, T., et al. 2012, PoS, 152
Cutler, C., Apostolatos, T. A., Bildsten, L., et al. 1993, PhRvL, 70, 2984
Cutler, C., & Flanagan, É. E. 1994, PhRvD, 49, 2658
Dalal, N., Holz, D. E., Hughes, S. A., & Jain, B. 2006, PhRvD, 74, 063006
Del Pozzo, W. 2012, PhRvD, 86, 043011
Dessart, L., Ott, C. D., Burrows, A., Rosswog, S., & Livne, E. 2009, ApJ, 690, 1681
Drake, A. J., Djorgovski, S. G., Mahabal, A., et al. 2009, ApJ, 696, 870
Droz, S., Knapp, D. J., Poisson, E., & Owen, B. J. 1999, PhRvD, 59, 124016
East, W. E., & Pretorius, F. 2012, ApJL, 760, L4
East, W. E., Pretorius, F., & Stephens, B. C. 2012, PhRvD, 85, 124009
Eichler, D., Livio, M., Piran, T., & Schramm, D. N. 1989, Natur, 340, 126
Enrico Petrillo, C., & Dietz, A. 2012, arXiv:1202.0804
Evans, P. A., Fridriksson, J. K., Gehrels, N., et al. 2012, ApJS, 203, 28
Fairhurst, S. 2011, CQGra, 28, 105021
Fairhurst, S. 2012, arXiv:1205.6611
Finn, L. S. 1992, PhRvD, 46, 5236
Finn, L. S., & Chernoff, D. F. 1993, PhRvD, 47, 2198
Flanagan, É. É., & Hughes, S. A. 1998, PhRvD, 57, 4535
Fong, W.-f., Berger, E., & Fox, D. B. 2010, ApJ, 708, 9
Fong, W.-f., Berger, E., Margutti, R., et al. 2012, ApJ, 756, 189
Foucart, F. 2012, PhRvD, 86, 124007
Foucart, F., Duez, M. D., Kidder, L. E., & Teukolsky, S. A. 2011, PhRvD, 83, 024005
Fox, D. B., Frail, D. A., Price, P. A., et al. 2005, Natur, 437, 845
Frail, D. A., Kulkarni, S. R., Ofek, E. O., Bower, G. C., & Nakar, E. 2012, ApJ, 747, 70
Green, J., Schechter, P., Baltay, C., et al. 2012, arXiv:1208.4012
Grupe, D., Burrows, D. N., Patel, S. K., et al. 2006, ApJ, 653, 462
Hadjiyska, E. I., Rabinowitz, D., Baltay, C., et al. 2011, BAAS, 43, 433.18
Hansen, B. M. S., & Lyutikov, M. 2001, MNRAS, 322, 695
Harry, G. M., & the LIGO Scientific Collaboration, 2010, CQGra, 27, 084006
Harry, I. W., & Fairhurst, S. 2011, CQGra, 28, 134008
Hirata, C. M., Gehrels, N., Kneib, J.-P., et al. 2012, arXiv:1204.5151
Hjorth, J., Watson, D., Fynbo, J. P. U., et al. 2005, Natur, 437, 859
Kanner, J., Camp, J., Racusin, J., Gehrels, N., & White, D. 2012, ApJ, 759, 22
Kasliwal, M. M. 2011, PhD thesis, California Institute of Technology
Kasliwal, M. M., Kulkarni, S. R., Gal-Yam, A., et al. 2012, ApJ, 755, 161
Kelley, L. Z., Ramirez-Ruiz, E., Zemp, M., Diemand, J., & Mandel, I. 2010, ApJL, 725, L91
Klimenko, S., Vedovato, G., Drago, M., et al. 2011, PhRvD, 83, 102001
Komatsu, E., Dunkley, J., Nolta, M. R., et al. 2009, ApJS, 180, 330
Kulkarni, S., & Kasliwal, M. M. 2009, in Astrophysics with All-Sky X-Ray Observations, ed. N. Kawai, T. Mihara, M. Kohama, & M. Suzuki (Wako: RIKEN and JAXA), 312
Kulkarni, S. R. 2005, arXiv:astro-ph/0510256
Kulkarni, S. R. 2012, arXiv:1202.2381
Kyutoku, K., Okawa, H., Shibata, M., & Taniguchi, K. 2011, PhRvD, 84, 064018
Law, N. M., Kulkarni, S. R., Dekany, R. G., et al. 2009, PASP, 121, 1395
Leaman, J., Li, W., Chornock, R., & Filippenko, A. V. 2011, MNRAS, 412, 1419
Lewis, A., & Bridle, S. 2002, PhRvD, 66, 103511
Li, L.-X., & Paczyński, B. 1998, ApJL, 507, L59
Li, W., Chornock, R., Leaman, J., et al. 2011a, MNRAS, 412, 1473
Li, W., Leaman, J., Chornock, R., et al. 2011b, MNRAS, 412, 1441
LIGO Scientific Collaboration, et al. 2012a, A&A, 539, A124
LIGO Scientific Collaboration, et al. 2012b, ApJ, 760, 12
Lindblom, L. 2009, PhRvD, 80, 042005
LSST Science Collaborations, et al. 2009, arXiv:0912.0201
Metzger, B. D., & Berger, E. 2012, ApJ, 746, 48
Metzger, B. D., Martínez-Pinedo, G., Darbha, S., et al. 2010, MNRAS, 406, 2650
Metzger, B. D., Piro, A. L., & Quataert, E. 2008, MNRAS, 390, 781
Metzger, B. D., Piro, A. L., & Quataert, E. 2009, MNRAS, 396, 304
Nakar, E. 2007, PhRp, 442, 166
Nakar, E., & Piran, T. 2011, Natur, 478, 82
Narayan, R., Paczynski, B., & Piran, T. 1992, ApJL, 395, L83
Nissanke, S., Holz, D. E., Hughes, S. A., Dalal, N., & Sievers, J. L. 2010, ApJ, 725, 496 (N10)
Nissanke, S., Sievers, J., Dalal, N., & Holz, D. 2011, ApJ, 739, 99 (N11)
Nuttall, L. K., & Sutton, P. J. 2010, PhRvD, 82, 102002
Owen, B. J. 1996, PhRvD, 53, 6749
Paczynski, B. 1991, AcA, 41, 257
Phinney, E. S. 1991, ApJL, 380, L17
Phinney, E. S. 2009, arXiv:0903.0098
Piran, T., Nakar, E., & Rosswog, S. 2013, MNRAS, in press (arXiv:1204.6242)
Piro, A. L. 2012, ApJ, 755, 80
Pretorius, F. 2005, PhRvL, 95, 121101
Pshirkov, M. S., & Postnov, K. A. 2010, Ap&SS, 330, 13
Rantsiou, E., Kobayashi, S., Laguna, P., & Rasio, F. A. 2008, ApJ, 680, 1326
Raymond, V., van der Sluys, M. V., Mandel, I., et al. 2009, CQGra, 26, 114007
Rezzolla, L., Giacomazzo, B., Baiotti, L., et al. 2011, ApJL, 732, L6
Roberts, L. F., Kasen, D., Lee, W. H., & Ramirez-Ruiz, E. 2011, ApJL, 736, L21
Rosswog, S., Liebendörfer, M., Thielemann, F.-K., et al. 1999, A&A, 341, 499
Rosswog, S., Ramirez-Ruiz, E., & Davies, M. B. 2003, MNRAS, 345, 1077
Ruffert, M., Janka, H.-T., Takahashi, K., & Schaefer, G. 1997, A&A, 319, 122
SASIR. 2012, http://www.sasir.org/
Sathyaprakash, B., et al. 2012, https://dcc.ligo.org/cgi-bin/DocDB/ShowDocument?docid=91470
Schutz, B. F. 2011, CQGra, 28, 125023
Shapiro, S. L., & Teukolsky, S. A. 1983, Black Holes, White Dwarfs, and Neutron Stars: The Physics of Compact Objects (New York: Wiley-Interscience)
Shibata, M., Kyutoku, K., Yamamoto, T., & Taniguchi, K. 2009, PhRvD, 79, 044030
Shibata, M., & Taniguchi, K. 2008, PhRvD, 77, 084015
Sigg, D., & the LIGO Scientific Collaboration. 2008, CQGra, 25, 114041
Singer, L., Price, L., & Speranza, A. 2012, ApJ, submitted (arXiv:1204.4510)
Soderberg, A. M., Berger, E., Kasliwal, M., et al. 2006, ApJ, 650, 261
Somiya, K. 2012, CQGra, 29, 124007
Stubbs, C. W. 2008, CQGra, 25, 184033
Taniguchi, K., Baumgarte, T. W., Faber, J. A., & Shapiro, S. L. 2007, PhRvD, 75, 084005
Tsang, D., Read, J. S., Hinderer, T., Piro, A. L., & Bondarescu, R. 2012, PhRvL, 108, 011102
van der Sluys, M., Raymond, V., Mandel, I., et al. 2008, CQGra, 25, 184011
van Eerten, H. J., & MacFadyen, A. I. 2011, ApJL, 733, L37
van Eerten, H. J., van der Horst, A., & MacFadyen, A. 2012, ApJ, 749, 44
Veitch, J., Mandel, I., Aylott, B., et al. 2012, PhRvD, 85, 104045
Vitale, S., Del Pozzo, W., Li, T. G. F., et al. 2012, PhRvD, 85, 064034
Wanajo, S., & Janka, H.-T. 2012, ApJ, 746, 180
Wen, L., & Chen, Y. 2010, PhRvD, 81, 082001